Research Square

Preprints are preliminary reports that have not undergone peer review.
They should not be considered conclusive, used to inform clinical practice,
or referenced by the media as validated information.

Load recovery at fixed deflection after creep relaxation in bending as a test of anelastic back-stress laws

Yo-Lun Yang

y.yang@ntut.edu.tw

National Taipei University of Technology

Research Article

Keywords:

Posted Date: November 14th, 2026

DOI: https://doi.org/10.21203/rs.3.rs-11550281/v1

License: This work is licensed under a Creative Commons Attribution 4.0 International License.
Read Full License

Additional Declarations: No competing interests reported.

Load recovery at fixed deflection after creep relaxation in bending as a test of anelastic back-stress laws

Yo-Lun Yang*

Graduate Institute of Manufacturing Technology, National Taipei University of Technology, 1 Sec. 3 Zhongxiao E. Rd., Taipei, 106344, Taiwan

Abstract

Creep-ageing models treat unloading as elastic, although part of the strain accumulated on the die keeps returning after release. A bending test is introduced in which a bar is unloaded to zero load after an eight-hour relaxation and the deflection is held for six hours while the load recovers, a response not previously recorded in bending. Eleven such tests on three thicknesses, with uniaxial recovery at zero stress and at fixed strain, give recovery under three conditions of constraint. A six-parameter back-stress law identified on three uniaxial creep and recovery histories is applied without refitting to the other two. The law describes the relaxation on the die, and the amplitude of the recovery transfers to bending, whereas the law returns the load at 1.3 to 3.5 times the measured half-time. The records after unloading determine the time scale of the recoverable strain, and the measured recovery saturates with hold duration where the law continues to rise. The dependence on hold duration has a candidate in a back-stress stiffness rising during the hold as the mobile dislocation density falls. For a die-clamped 5 mm section, the law projects a delayed springback of 16 to 18 % of the elastic springback after thirty days, and retaining that shape requires 10 to 42 % more die curvature than compensation at release. Recovery after unloading therefore provides a separate test for a constitutive law that is to predict the retained shape of a formed part.

Keywords: creep-ageing, anelasticity, back stress, stress relaxation, springback, constitutive identification

1. Introduction

Creep-age forming holds a plate against a die at the ageing temperature of a precipitation-hardening alloy, lets the stress relax for several hours and releases it with a residual curvature (Ho et al., 2004b; Lam et al., 2015b; Lin et al., 2006; Liu et al., 2026; Zhan et al., 2011; Zhang et al., 2022). Springback at release removes most of the imposed shape. Reported springback ratios run from 53 to 68 % for 0.8 to 1.6 mm AA2024 sheet (Başpınar et al., 2026) to 80 to 93 % for 2 to 6 mm aluminium–lithium strips (Wang et al., 2023). Die compensation addresses this springback by iterating a finite element model or a closed-form section solution until the released shape meets the target (Li et al., 2019b; Wang et al., 2023). Both procedures target the shape at die release. Recovery, however, continues after release. A fraction of the strain

*Corresponding author.
Email address: y.yang@ntut.edu.tw (Yo-Lun Yang)

accumulated during the hold is recoverable and keeps returning at zero load (Yang, 2017). At room temperature, springback in formed aluminium sheet also grows approximately with the logarithm of time for months, by up to a fifth of its eventual value (Lim et al., 2008; Wang et al., 2004). The ranking of alloys by this delayed springback does not follow their creep strains (Hama et al., 2020). The delayed springback is larger in aluminium than in high-strength steel and increases with the duration of the bending hold (Matsugi and Hino, 2024). A constitutive law for the process must therefore describe not only the stress relaxation on the die but also how much relaxed strain returns, how fast and under which constraint.

The returning strain is anelastic in the sense of Zener, i.e. time-dependent and recoverable (Nowick and Berry, 1972; Zener, 1948). An internal stress stored during forward creep drives the recovery (Gibeling and Nix, 1981), and the creep runs backwards once the applied stress is removed (Gibeling and Nix, 1981; Lloyd and McElroy, 1974), with a logarithmic time law in pure aluminium (Cottrell, 1952; Shen et al., 2011). In a precipitation-hardened alloy, dislocations bowed between non-shearable particles store the internal stress as a Bauschinger stress. Reverse loading of an over-aged 7xxx alloy gives Bauschinger stresses of 50 to 200 MPa (Fribourg et al., 2011). Particle-scale models describe this internal stress (Bhattacharyya et al., 2019; Daroju et al., 2022; Myhr et al., 2020), which drives nonlinear anelastic strain in unloaded sheet (Arechabaleta et al., 2016; Torkabadi et al., 2018).

Three families of constitutive description are in use for the anelastic strain. Linear Kelvin elements in series with the permanent creep strain (Hart, 1976; Sinha, 2003) are still fitted to recovery at zero stress, singly (Tulkki and Ikonen, 2015), as a double exponential (Nardone et al., 1985) or with a power law (Dandrea and Lakes, 2009). With a positive spectrum of retardation times, the elements give an approximately logarithmic recovery over a finite window (Mainardi and Spada, 2012). A back stress of the Armstrong–Frederick type (Armstrong and Frederick, 1966; Chaboche, 2008; Ohno and Wang, 1993) drives a reverse viscoplastic flow once the applied stress falls below it. The state-variable and overstress descriptions allow that flow at any nonzero back stress (Bodner and Partom, 1975; Freed and Walker, 1993; Hart, 1976; Krempl, 2003; Miller, 1976), whereas the Perzyna and Chaboche descriptions stop it when the back stress falls inside the yield radius (Chaboche, 1993; Lemaitre and Chaboche, 1990; Perzyna, 1966). Either form can be derived with the back stress represented through the free energy (Germain et al., 1983; Halphen and Nguyen, 1975; Le and Tran, 2018). Creep-ageing models in the back-stress family commonly add an ageing-dependent yield-type threshold (Ho et al., 2004a; Li et al., 2017b). A nonzero elastic limit is compatible with stress recovery after unloading of a high-strength steel but not with partial unloading inside the elastic domain (Matsugi and Hino, 2025). For cast aluminium, a back-stress form was rejected because its threshold produces an abrupt transition (Dandrea and Lakes, 2009). A recovery test at zero stress separates a reverse flow without a threshold from one with a threshold.

Current creep-ageing and stress-relaxation-ageing models describe anisotropy, evolving strength, pre-deformation and loading history (Rong et al., 2021; Wang et al., 2022, 2024, 2025;

Xu et al., 2025; Yang et al., 2025; Zhou et al., 2026) and connect the relaxation kinetics with mobile dislocation density and precipitation (Lao et al., 2023; Lee et al., 2021a; Li et al., 2019a; Lyu et al., 2020; Nguyen et al., 2026). The same models treat unloading as reversed elastic loading (Wang et al., 2023, 2024). Most of them include a threshold that gives zero creep rate at zero applied stress, so that recovery after die release is excluded by construction. Post-release recovery is also absent from the two reviews of creep-age forming cited above (Liu et al., 2026; Zhang et al., 2022). The relaxation literature on AA7050 itself, however, reports observations that a stored internal stress would explain. Multi-step relaxation at 177 °C proceeds with no apparent threshold (Zheng et al., 2018, 2023). Creep-ageing under load control and relaxation-ageing under strain control give different rates and stress exponents (Zheng et al., 2023, 2017). Repeated relaxation gives a negative apparent stress exponent in the plastic region (Li and Shi, 2022). Under elastic loading, the second relaxation stage shows a stress rebound at fixed strain (Zhang et al., 2025).

Layer models of the bent section integrate the creep law through the thickness and also superpose an elastic unloading from the end-of-ageing moment (Ho et al., 2004b; Jeunechamps et al., 2006; Wang et al., 2023). Springback decreases with thickness (Başpınar et al., 2026; Li et al., 2018a; Wang et al., 2023), whereas inherited residual stress can increase or decrease it (Lam et al., 2015a; Li et al., 2018b). Finite element models predict compressive surfaces and a tensile core after forming (Li et al., 2017a). Including inherited stress improves their shape predictions (Li et al., 2023; Yu et al., 2026). Through-thickness variation also matters because thick 7050 plate creeps faster at the surface than at the centre (Bian et al., 2020). None of these models carries a recovery term after unloading. Bending relaxation is a standardised test (ASTM International, 2021), but no published bending test known to the author holds the deflection after unloading and records the load that returns. The nearest are tubes relaxed at fixed curvature at room temperature (Lee et al., 2021b) and in-reactor three-point bending of austenitic steel (Zumpicchiat et al., 2025).

The records that supply the missing measurement were taken in the author's earlier study of AA7050-T6 at 174 °C (Yang, 2017). Only the creep-ageing and recovery tests (CART) and a dislocation-density model of the recovery have been published outside that work (Yang et al., 2017). The dislocation-density model (Yang, 2017; Yang et al., 2017) is also evaluated here against the same records. The CART tests record strain at zero stress. The creep-ageing and back-stress test (CABT) records stress at fixed strain. The stress-relaxation and back-stress bending test (SRBT) records load at fixed deflection after an eight-hour relaxation and unloading. Together, the three modes measure recovery under different boundary conditions. The SRBT then tests the transfer of a law identified over a narrow uniaxial stress range. Within each section, stress varies from the surface to the neutral axis, and the tests span a 4.6-fold stress range.

The transfer of a back-stress law identified from uniaxial creep and recovery to constrained bending is investigated here without constitutive refitting. The comparison with the bending

records identifies the features of recovery that the records distinguish and the parameters that bending constrains beyond the uniaxial identification. A separate free-springback calculation then follows the retained curvature and the required die compensation as recovery continues to a specified assessment time. The two parts connect the identification of a recovery law with its use in forming, while keeping measured reaction recovery apart from projected shape evolution.

2. Experimental procedure

2.1. Material and apparatus

All specimens were cut along the rolling direction from AA7050-T6 plate (Yang, 2017). The starting material, designated AA7050-T6 here, is termed AA7050-TAF in the earlier study. The material was solution-treated at 477 °C for one hour and water-quenched. Ageing followed at 121 °C for eight hours and then at 165 °C for one hour (Yang, 2017). The nominal composition in wt% was Zn 6.25, Mg 2.14, Cu 2.23, Fe 0.05, Si 0.03 and other elements 0.15, with aluminium as the balance. The Young's modulus at 174 °C, $E = 65.2$ GPa, is taken from the earlier study. The tests used an Instron 5584 frame with a 150 kN load cell and an oven for which the earlier study reports a temperature band of 2 °C. The load cell has a quoted accuracy of 20–40 N, whereas the short-term noise estimated from the records is smaller.

The drawing of the uniaxial specimen in the earlier study gives a nominal gauge diameter of 8 mm and a parallel length of 36 mm. All uniaxial load-to-stress conversions use the circular gauge section of 50.2654 mm^2.

The bending bars were 150 mm long, 25 mm wide and 3, 5 or 8 mm thick. The bars were loaded in a three-point rig with rollers of 10 mm diameter at a nominal span of 140 mm (Fig. S1).

2.2. Test procedures

The three test modes are sketched in Fig. 1. The uniaxial tests, twelve CART and one CABT, are listed in Table 1 and the eleven SRBT in Table 2.

In the CART series the specimen was loaded to the hold stress, held, unloaded, and the strain was recorded at zero stress throughout the recovery period. The hold stresses were 137.5, 150 and 162.5 MPa and the hold times 2, 4, 6 and 8 hours, giving twelve tests. In the CABT series the specimen was crept and unloaded in the same way, after which the extensometer strain was held at the value reached at the end of unloading and the holding load was recorded. The record used here is the CABT at 162.5 MPa and 8 hours.

In the SRBT series the crosshead was driven at 4 mm/min (0.0667 mm/s) to a deflection δ_0 and held for 8 hours while the load relaxed from F_{app} to $F_{8\mathrm{h}}$. The crosshead was driven back at the same rate until the load reached zero at a deflection δ_1 and held at δ_1 for 6 hours while the load recovered. The crosshead was then returned at about 1 mm/min. The deflection δ_2 is the crosshead position at which the load returned to zero on this last movement. The first ramp, to δ_0, took 17–118 s. The surface stress at F_{app} is $\sigma_s = 3F_{\mathrm{app}}L/(2bh^2)$ from classical beam theory, with the effective span L, the bar width b and the thickness h. The eleven tests span surface

stresses of 95–442 MPa and ratios δ_0/h from 0.14 to 2.6. The recorded crosshead histories give the stated ramp rate in every test, whereas the earlier study reports 0.2 mm/s, equivalent to 12 mm/min (Yang, 2017). The calculations follow the recorded histories.

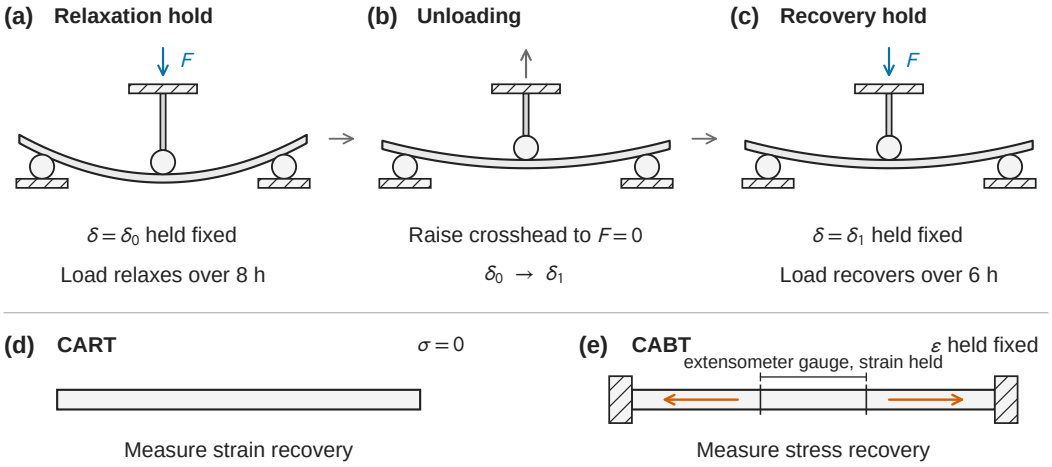


Figure 1: Test protocols at 174 °C, drawn schematically and not to scale. (a–c) The bending bar is held at the crosshead deflection δ_0 while the load relaxes, unloaded to zero force at δ_1 and held there while the load recovers. (d, e) The uniaxial specimen recovers at zero stress in the creep-ageing and recovery test (CART) and at fixed extensometer strain in the creep-ageing and back-stress test (CABT).

Table 1: The thirteen uniaxial tests. Columns give the inelastic strain ε_{in} at the end of the hold and the strain recovered at zero stress in the first 6 hours, with its share of ε_{in}. The last two columns give the length of the record after unloading and the source of the record.

test	mode	σ (MPa)	hold (h)	ε_{in} (%)	recovered in 6 h (%)	share (%)	record (h)	source
1	CART	137.5	2	0.041	0.034	83	13.3	traced
2	CART	137.5	4	0.052	0.036	70	12.0	traced
3	CART	137.5	6	0.056	0.034	60	10.0	traced
4	CART	137.5	8	0.067	0.031	47	8.0	traced
5	CART	150	2	0.046	0.036	78	6.0	traced
6	CART	150	4	0.060	0.044	73	6.0	traced
7	CART	150	6	0.070	0.041	58	6.1	traced
8	CART	150	8	0.076	0.026	35	8.0	traced
9	CART	162.5	2	0.061	0.042	69	8.1	traced
10	CART	162.5	4	0.078	0.038	49	10.0	traced
11	CART	162.5	6	0.091	0.033	36	8.6	traced
12	CART	162.5	8	0.105	0.036	34	8.9	raw
13	CABT	162.5	8	–	–	–	13.5	raw

ε_{in} is the measured strain less σ/E. Sources are the machine record (raw) and the plotted record of the earlier study read from the figure (traced). For the CABT the recorded quantity is the stress at fixed strain, evaluated over the first eight hours of recovery.

2.3. Data reduction

The CART and CABT procedures and records are those of the earlier study (Yang, 2017). The CART at 162.5 MPa and 8 hours is used as recorded, and the other eleven CART curves

Table 2: The eleven bending tests. Surface stress $\sigma_s = 3F_{\text{app}}L/(2bh^2)$ with $L = 141.8$ mm and $b = 25$ mm, and relaxation $1 - F_{8\text{h}}/F_{\text{app}}$. ΔF is the rise in load during the 6 hour recovery hold, u its noise, and δ_2 the position at which the load returns to zero on the final movement. All values come from the raw records.

test	h (mm)	σ_s (MPa)	δ_0 (mm)	F_{app} (N)	$F_{8\text{h}}$ (N)	relax. (%)	δ_1 (mm)	$\Delta F \pm u$ (N)	δ_2 (mm)	δ_0/h
1	3	95	2.00	100.4	70.8	29.5	0.84	6.7 ± 1.2	0.77[†]	0.67
2	3	347	5.47	366.9	215.5	41.3	2.10	19.2 ± 1.5	1.59	1.82
3	3	421	7.88	445.3	303.1	31.9	3.75	27.8 ± 0.8	3.24	2.63
4	5	125	1.28	366.8	246.7	32.7	0.38	14.0 ± 1.6	0.31	0.26
5	5	175	2.00	512.9	396.3	22.7	0.69	24.6 ± 1.1	0.57	0.40
6	5	253	3.00	744.8	518.5	30.4	0.89	39.7 ± 0.4	0.69	0.60
7	5	360	4.00	1058.3	739.7	30.1	1.30	48.2 ± 0.3	1.02	0.80
8	5	442	4.90	1300.2	835.3	35.8	1.84	62.1 ± 0.3	1.46	0.98
9	8	142	1.11	1065.6	846.5	20.6	0.25	42.6 ± 0.4	0.19	0.14
10	8	292	2.00	2193.2	1630.3	25.7	0.52	76.5 ± 0.4	0.40	0.25
11	8	433	3.31	3256.4	2202.6	32.4	1.21	137.4 ± 0.3	1.00	0.41

[†] In test 1 the record ends 4.2 s after the start of the final movement with the load at 0.78 N and the crosshead at 0.748 mm. The 5-point median of the load first falls to 1.5 N at 0.774 mm and the first raw sample at or below 1 N lies at 0.776 mm, so δ_2 lies between 0.75 and 0.78 mm. In test 8 the record ends at the first sample with the load below 1 N.

are traced from the plotted results of that study. The 8 hour holds at 137.5 and 150 MPa are represented by the midpoint of the band formed at each stress by the 2, 4, 6 and 8 hour tests while on load. Inelastic strain is the measured strain less σ/E.

The CABT recorded time and load at intervals of at most 3 s through loading, the hold, unloading and recovery. Recovery time is counted from the end of unloading, at the local minimum of the load. The record continues for 13.5 hours after unloading, and comparisons use the first eight hours. The stress needed to hold the strain reaches 13.6 MPa after four hours and 14.4 MPa after eight hours, with a further rise outside the comparison window. CABT rms errors are evaluated at uniform 3 s intervals over the eight-hour window, with the record interpolated between samples.

The eleven bending tests recorded time, crosshead displacement and load through every stage (Fig. 2, unfiltered in Fig. S2). The relaxation holds lasted 8 hours to within 0.3 s, the recovery holds between 5.94 and 6.03 hours, and the crosshead moved by less than 1×10^{-4} mm during a recovery hold.

Each bending record is reduced to the loads and deflections of Table 2. The loads F_{app} and $F_{8\text{h}}$ are taken at the end of the first ramp and at the end of the relaxation hold, and the relaxation is $1 - F_{8\text{h}}/F_{\text{app}}$. The rise in load during the recovery hold is ΔF. The rise is measured on the 15-point running median of the load, from 60 s after the start of the hold to 2 s before the final movement. Under an independent-sample approximation, the uncertainty of ΔF is $u = \sqrt{\pi/15}\, s_F$. Here s_F is the standard deviation of the load about its running median in the last ten minutes of the hold. The noise u is 0.3 to 1.6 N (Table 2) and bounds the short-term scatter only. A constant offset of the load cell cancels in ΔF, whereas a slow drift over the six-hour hold does not. The records carry time, crosshead and load only, so that a drift of the cell cannot

be separated from the recovery. The drift of 2 N over six hours carried through Section 6.3 is therefore an assumed scale and not a measured bound.

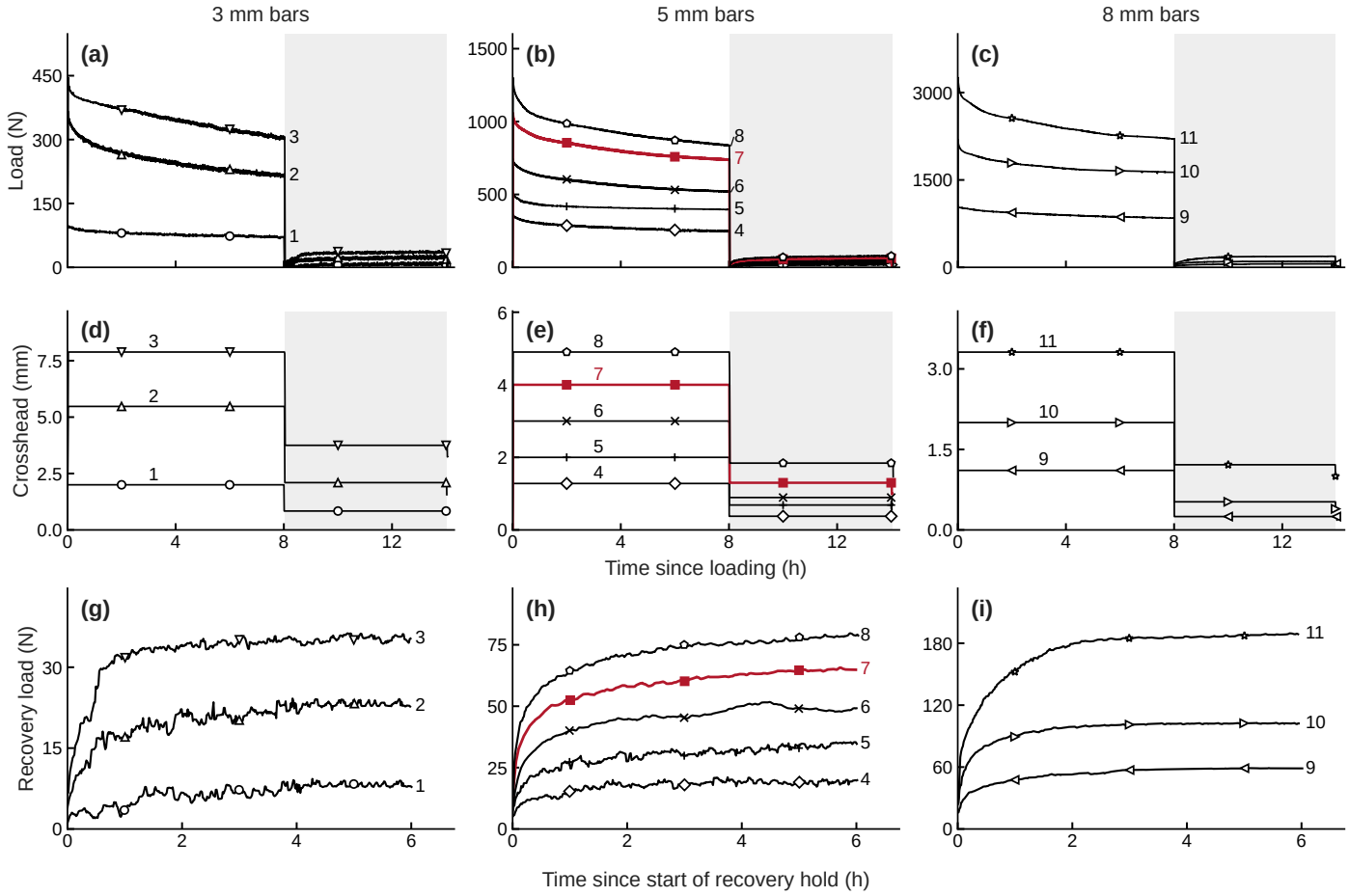


Figure 2: Records of the eleven bending tests grouped by bar thickness. (a–c) Load and (d–f) crosshead displacement through the test, with the recovery hold shaded, and (g–i) load during the recovery hold as three-minute running medians. Test 7 is drawn in solid red with filled squares throughout the article, and every other test keeps the marker assigned here wherever individual records are plotted. The open symbols are instead grouped by thickness in Figs. 3e, 5c and 6. An isolated 0.8 s downward excursion of the test 1 load about one hour into the recovery hold is left out of the running median in this display only.

2.4. Rig stiffness and repeatability

The loading and unloading ramps of the same eleven records provide 22 stiffness values. The 22 values are fitted jointly to a beam with shear compliance in series with a constant machine compliance. The fit gives an effective span $L = (141.8 \pm 1.7)$ mm, compared with the nominal 140 mm, and a machine compliance $C_m = (1.06 \pm 0.61) \times 10^{-4}$ mm/N. Every calculation uses these fitted values. At each stress the four tests on load together during the first 1.93 hours span a band of 10 to 17 % of the inelastic strain at 1.3 hours. Repeats of tests 2 and 5 differ from the original tests in relaxation by 4.8 and 7.1 percentage points. The fits with other stiffness windows, the toe of each ramp and the repeatability records are in Section S7.

2.5. Experimental results

The same ramps and holds give four measures for each bending test (Table S21). The instantaneous springback $(\delta_0 - \delta_1)/\delta_0$ is the elastic part of unloading. The final protocol springback $(\delta_0 - \delta_2)/\delta_0$ includes the recovery hold. The deflection recovery $(\delta_1 - \delta_2)/\delta_1$ measures the further return of the bar during the final movement. The load recovery $\Delta F/[k_0(\delta_0 - \delta_1)]$ expresses the rise during the hold as a fraction of the nominal unloading excursion, with $k_0 = F_{\text{app}}/\delta_0$.

The load relaxes by 20.6–41.3 % in 8 hours, and the relaxation does not order with thickness at matched stress. At 421, 442 and 433 MPa the 3, 5 and 8 mm bars relax by 31.9, 35.8 and 32.4 %. The instantaneous springback is 52–78 % and the final protocol springback 59–83 %.

The load recovers during the hold by 3.5–6.7 % of F_{app} (Fig. S3). Relative to the nominal unloading excursion, the rise is 4.7–7.6 % for the 5 and 8 mm bars and 8.5–11.9 % for the 3 mm bars. At the matched stresses, the load recovery of the 3, 5 and 8 mm bars is 11.92, 7.65 and 6.66 %, so the two thicker bars differ by 1.0 percentage point. Released after the hold, the bar returns by a further 7.6–25.2 % of the held deflection δ_1, equal to 5.5–14.9 % of the elastic springback $\delta_0 - \delta_1$.

Use of AI tools

ChatGPT (OpenAI) and Claude (Anthropic) were used as coding assistants to prepare the figures from the measured data and to edit the text for clarity. The author checked all output and takes full responsibility for the content.

3. Recovery under three conditions of constraint

Recovery continues after unloading under zero stress, fixed strain and fixed deflection, and each control records it in its own quantity (Fig. 3a–c). The records are drawn against the law of Section 4 identified on the CART histories alone, the CART-only law, so that each can be read as a test of it. At zero stress the strain decreases, whereas the reaction stress at fixed strain and the load at fixed deflection rise. Every bending record rises through the six-hour hold, with short-term noise about a monotonic trend.

Normalised by its final recovery, each record is approximately logarithmic in time over part of its resolved window, and the three records do not collapse onto one curve. Half-times counted to the end of each record depend on where that record starts and ends, and so do not rank the constraints (Section S14). Since the recovered fraction depends on its starting and final times, it follows that the rates must be compared over a common observation window.

Over a common window, recovery after the same eight-hour hold at 162.5 MPa takes 2.5 times as long at fixed strain as at zero stress. Half of the six-hour change, counted from 60 s, is reached after 1126 s at zero stress and 2787 s at fixed strain, each evaluated on the 15-point running median (Fig. 3d). At fixed deflection the half-time shortens from 4075 s after the 95 MPa hold of test 1 to 630–1423 s after the seven holds above 250 MPa (Fig. 3e). The stored strain therefore returns at a rate set by the constraint and by the stress of the preceding hold. A law

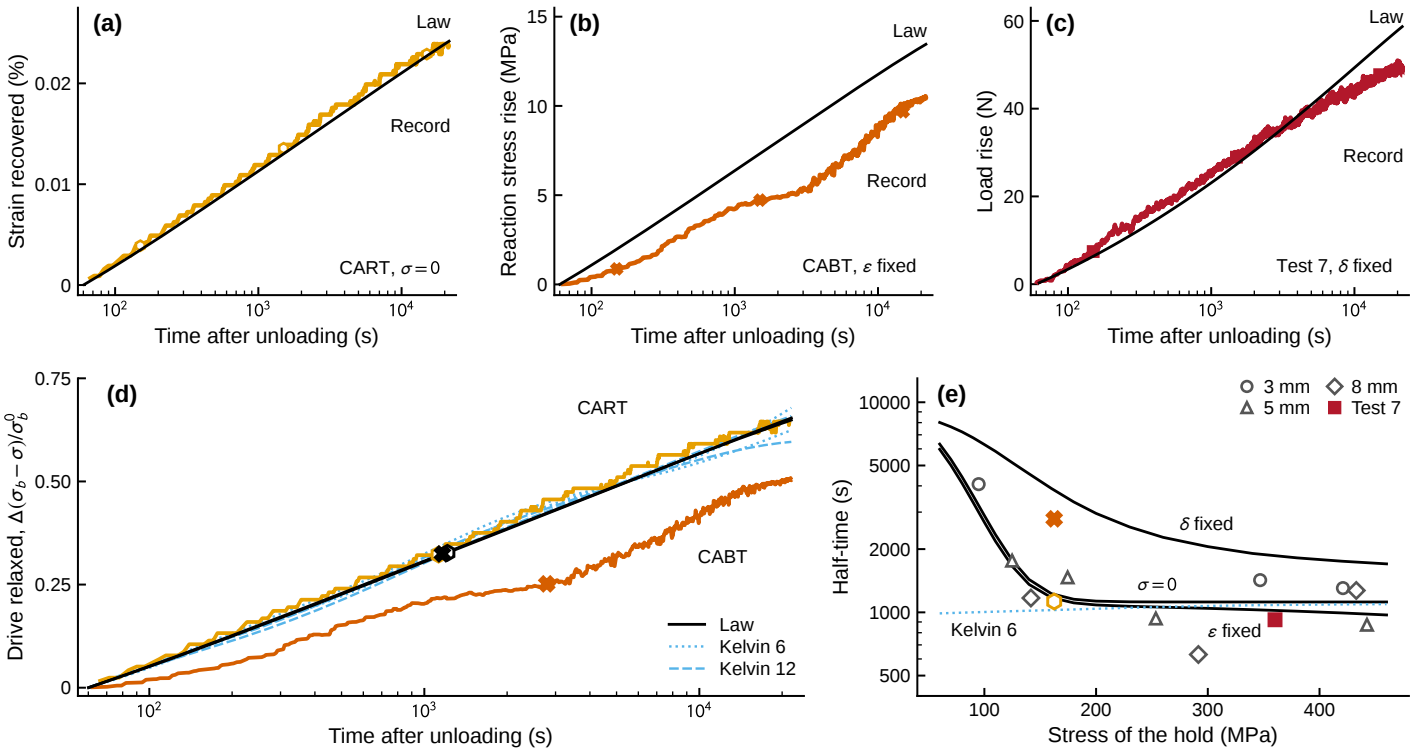


Figure 3: Recovery after unloading at 174 °C under three controls, with the back-stress law identified on the three creep-ageing and recovery (CART) histories and applied without refitting in black. (a) Strain recovered at zero stress and (b) reaction stress at fixed strain after eight hours at 162.5 MPa, and (c) load at fixed deflection in bending test 7. Each is counted from its value 60 s after unloading, and the records are 15-point running medians on a logarithmic time axis. (d) Drive on the back-stress element relaxed since 60 s at zero stress and fixed strain, as a fraction of the back stress of 147 MPa at unloading. The six- and twelve-mode Kelvin spectra fitted to the same histories are in blue, and a marker on each curve sits at its half-time. The record curves in (d) are the strain and stress of (a) and (b) converted to drive through the stiffness H and the modulus E of the law. (e) Half-time of the change from 60 s to six hours against the stress of the hold for the thirteen records, the bar stress being the nominal surface stress. Curves give the law for each control after an eight-hour hold and the six-mode spectrum at fixed deflection.

transferred between the controls must reproduce not only the amplitude of the recovery under each control but also its time scale.

The amplitude of the fixed-strain reaction measures the recoverable strain stored at unloading through the elastic modulus E and the back-stress stiffness H in series. With ε_b^0 the recoverable strain at unloading and the permanent strain frozen, the limiting reaction is $EH\varepsilon_b^0/(E+H)$. The back stress at unloading is instead $H\varepsilon_b^0$. Thus the CABT reaction of 14.4 MPa at eight hours differs from the back stress at unloading, which the law estimates as 147 MPa. The reaction still rises by 0.8 MPa between four and eight hours, so it is a stage of a continuing recovery and not an equilibrium value (Section 4.3).

The logarithmic tendency, the rising fixed-strain reaction and the monotonic six-hour bending recovery are reproduced by the back-stress law and by positive Kelvin spectra alike. The records therefore establish only that a law with a back stress and no reverse-flow threshold reproduces broad recovery trends across the three conditions, while leaving discrepancies in

amplitude and rate.

4. Constitutive model

4.1. Formulation

The law is the one-dimensional element of Fig. 4. The total strain is the sum of an elastic part, a recoverable part ε_b and a permanent part ε_v,

$$\varepsilon = \frac{\sigma}{E} + \varepsilon_b + \varepsilon_v. \tag{1}$$

The recoverable strain is carried by a back-stress element. A spring of stiffness H stores the back stress $\sigma_b = H\varepsilon_b$. A nonlinear dashpot in parallel with the spring flows at a rate set by the difference between the applied stress and the back stress,

$$\dot{\varepsilon_b} = A_b \sinh[B_b\,(\sigma - \sigma_b)], \qquad \sigma_b = H\,\varepsilon_b. \tag{2}$$

The permanent strain flows under the applied stress with a time-hardening factor of exponent p,

$$\dot{\varepsilon_v} = A_v \sinh(B_v\,\sigma)\,(1 + t/\tau_v)^{-p}. \tag{3}$$

The sinh kinetics, in which A_b and A_v are prefactors and B_b and B_v are stress sensitivities, are those of Garofalo (Garofalo, 1965). Time in the permanent branch runs continuously from initial loading through unloading and recovery. The time-hardening factor is the simplest representation of the decline in creep rate that the ageing alloy shows throughout the eight-hour hold. The time scale τ_v serves only to regularise the rate at $t = 0$. With τ_v fixed at 10 s, the factor behaves over the resolved window as the power law $(t/\tau_v)^{-p}$.

The recoverable branch, Eq. (2), contains no threshold. At zero applied stress the drive on the dashpot, $\sigma - \sigma_b$, is $-\sigma_b$, and the recoverable strain decreases. At fixed total strain, $\sigma = E(\varepsilon_{\mathrm{in}} - \varepsilon_b - \varepsilon_v)$, where $\varepsilon_{\mathrm{in}}$ is the inelastic strain at unloading. If permanent strain is frozen, the recoverable branch approaches rest at $\sigma = \sigma_b$. In the complete law, permanent flow continues under the recovered stress, so that the rest condition is not a time-independent equilibrium.

The law has the structure of a generalised standard material (Germain et al., 1983; Halphen and Nguyen, 1975). With the Helmholtz free energy $\psi = \frac{1}{2}E(\varepsilon - \varepsilon_b - \varepsilon_v)^2 + \frac{1}{2}H\varepsilon_b^2$, both flow rules follow from one convex dual dissipation potential (Section S8). The time-hardening factor scales the permanent-flow term of that potential by a positive function of time. The dissipation $\mathcal{D} = X_b\dot{\varepsilon_b} + X_v\dot{\varepsilon_v}$, with $X_b = \sigma - \sigma_b$ and $X_v = \sigma$ the forces conjugate to ε_b and ε_v, is non-negative for either sign of X_b, so recovery at zero stress satisfies the second law. A dead band on the flow is admissible too, and Section 5 tests it at fixed widths.

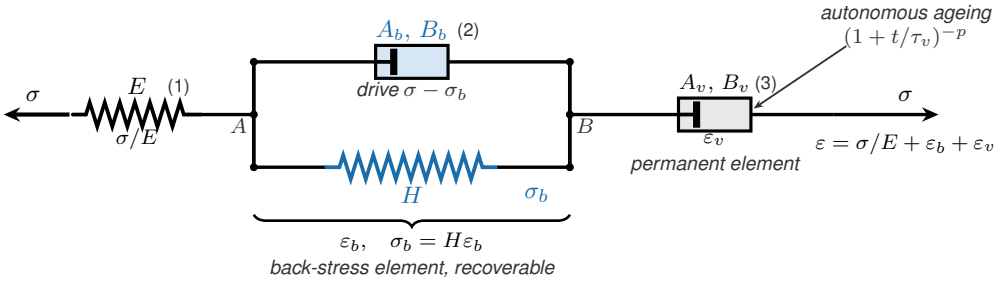


Figure 4: Rheology of the back-stress law, Eqs. (1)–(3), drawn in the network of Yang (2026). Between nodes A and B the back-stress element has a dashpot carrying the drive $\sigma - \sigma_b$ in parallel with a spring carrying $\sigma_b = H\varepsilon_b$. The permanent element in series has a rate that falls with time through the factor $(1 + t/\tau_v)^{-p}$. No rail has a threshold, so at $\sigma = 0$ the dashpot is driven by $-\sigma_b$ and flows backwards.

4.2. Determination of the constants

Without a dead band, the law contains seven constants in addition to E, of which τ_v is fixed at 10 s (Section 4.1) and the other six are identified. The identification comprises the three eight-hour CART hold and recovery histories, in which the holds at 137.5 and 150 MPa are represented by their band midpoints. The identification contains 204 residuals, comprising 84 hold points and 120 recovery points. The residuals are sampled approximately uniformly in $\log t$ and scaled by 10^4 in strain. The objective is half the sum of their squares. The objective is flat in τ_v below 100 s. The prefactor A_v and the exponent p are correlated, and the rate function they define together (Fig. S8d) is the identified quantity. Re-identification with band edges in place of the midpoints or with a shifted time origin tests the sensitivity of the identification (Section 7.3). Neither CABT nor bending enters this identification. The identified parameters are listed in Table 3.

Table 3: Parameters identified on the three 8 hour CART curves. τ_v is held at 10 s, within the range below 100 s where the objective is flat. The two joint identifications including bending add bending tests 3, 6, 10 or 4, 8, 9 to the identification set.

identification set	A_b (s^{-1})	B_b (MPa^{-1})	H (GPa)	A_v (s^{-1})	B_v (MPa^{-1})	p	τ_v (s)
CART only	1.24×10^{-9}	0.0591	397	6.28×10^{-9}	0.0288	0.41	10
+ SRBT 3, 6, 10	2.31×10^{-9}	0.0586	385	2.36×10^{-9}	0.0260	0.19	10
+ SRBT 4, 8, 9	2.74×10^{-9}	0.0577	398	3.42×10^{-9}	0.0249	0.21	10

The law reproduces the three holds (Fig. 5a). The rms residual over the hold stage is 0.0013–0.0027 % per curve at the sampling points of the objective. The identified back-stress stiffness is $H = 397$ GPa, so that $E/H = 0.164$ and the recoverable strain saturates at σ/H, which is 0.035, 0.038 and 0.041 % at the three stresses. The back stress rises to 0.7 of the applied stress within the first hour and to 0.9 at unloading, where it reaches 147 MPa. The drive therefore falls from 50 MPa at one hour to 16 MPa at the end of the hold. The recoverable strain at unloading is 0.037 %, close to its saturation value.

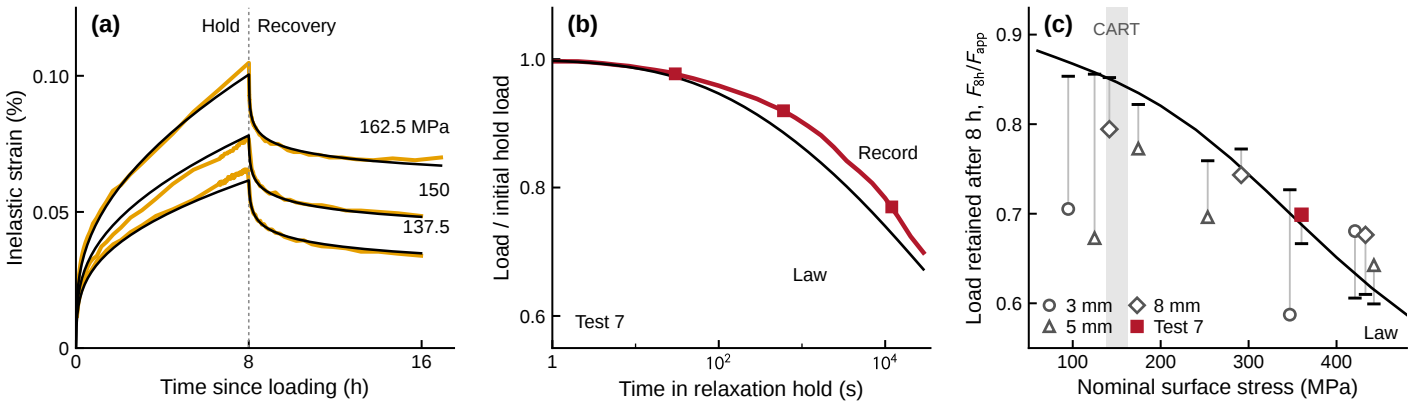


Figure 5: Identification of the back-stress law on the three creep-ageing and recovery (CART) records and its transfer to the relaxation hold in bending. (a) Inelastic strain through the eight-hour hold and recovery at 137.5, 150 and 162.5 MPa, records in colour and the law in black, with the law drawn continuously across unloading. (b) Load during the relaxation hold of test 7, normalised by its initial hold load. (c) Load retained after the hold against nominal surface stress, the law at each test being a black tick and over stress for an idealised 5 mm protocol the curve. The shaded band in (c) marks the CART stress range. The grey connectors in (c) join each record to the law at that test and show the difference between the two, not an uncertainty.

4.3. Analytical solutions

The recoverable branch, Eq. (2), integrates in closed form for homogeneous constant-stress or fixed-strain recovery with permanent flow suppressed. Let $K_d = H - \mathrm{d}\sigma/\mathrm{d}\varepsilon_b$ be the stiffness with which the drive on the dashpot falls as the recoverable strain returns. The stiffness K_d equals H at fixed stress and $E + H$ at fixed total strain with ε_v unchanged. With $s = B_b(\sigma_b - \sigma)$, positive during recovery, and K_d constant, the recoverable branch becomes

$$\frac{\mathrm{d}s}{\mathrm{d}t} = -\frac{\sinh s}{\tau_d}, \qquad \tau_d = \frac{1}{A_b B_b K_d}, \tag{4}$$

and for a body unloaded to zero stress at $t = 0$, with t now counted from unloading, from a back stress σ_b^0, separating the variables with $\int \mathrm{d}s/\sinh s = \ln\tanh(s/2)$ gives

$$\tanh\frac{s}{2} = \tanh\frac{s_0}{2}\,\exp\!\left(-\frac{t}{\tau_d}\right), \qquad s_0 = B_b\sigma_b^0. \tag{5}$$

At zero stress $K_d = H$ exactly and the permanent flow vanishes with the stress, so Eq. (5) with $s = B_b H\varepsilon_b$ is the full solution. At fixed strain, with $K_d = E + H$ and the permanent flow frozen, the solution gives the stress

$$\sigma = \frac{E}{E+H}\left(\sigma_b^0 - \frac{s}{B_b}\right), \tag{6}$$

and the element comes to rest, with $s = 0$ and $\sigma = \sigma_b$, at

$$\sigma_{\mathrm{rest}} = \frac{E}{E+H}\,\sigma_b^0. \tag{7}$$

For the 162.5 MPa hold this rest value is 20.7 MPa, above the 14.4 MPa measured at eight hours, where the record is still rising. With permanent flow retained, the complete law reaches a maximum reaction of 20.0 MPa after 29.6 h and then declines as the permanent flow continues under the recovered stress (Section S10). The measured eight-hour reaction, the rest value and the evolving back stress of the complete law are therefore three quantities distinct from one another and from the back stress at unloading.

The solution is logarithmic while $s \gg 1$. There $\sinh s \simeq \frac{1}{2}e^{s}$ and

$$s = s_0 - \ln\!\left(1 + \frac{t}{t^*}\right), \qquad t^* = 2\,\tau_d\, e^{-s_0}, \tag{8}$$

so that at zero stress the recoverable strain follows $\varepsilon_b^0 - \ln(1 + t/t^*)/(B_b H)$, a straight line in $\ln t$ with slope $1/(B_b H)$ that begins at t^*. For the identified parameters the slope is 0.00426 % per unit $\ln t$. The stress at fixed strain rises as $E \ln(1 + t/t^*)/[(E + H)B_b]$, which is 2.39 MPa per unit $\ln t$. The constants of the three eight-hour holds are listed in Table S22. The onset time t^* lies between 12 and 51 s, so the logarithmic stage covers nearly all of the recorded recovery.

The limiting time τ_d of Eq. (4) is 9.56 h at zero stress, where $K_d = H$, and 8.21 h at fixed total strain with permanent strain frozen, where $K_d = E + H$. The fixed-strain value applies near equilibrium with permanent flow suppressed, as derived in Section S15. The complete fixed-strain law includes permanent flow and must be integrated as a coupled system.

4.4. Uniaxial tests not used in the fitting

Integrated as such a system, the CART-only law predicts the recovery curves of the 2, 4 and 6 hour tests and the CABT. Specimens from the shorter CART tests also contribute to the pooled early hold bands used in the identification, so their complete histories are partial hold-outs. The inelastic strain at unloading of all twelve CART tests is compared with the model in Fig. S4b. The rms error over the nine hold-out tests is 0.0019 %. The strain recovered after unloading, counted from the first resolved point of each record, 2.7 to 5.6 minutes after unloading, is compared with the model in Fig. S4c. Measured values lie between 0.018 and 0.028 % and the model gives 0.018–0.021 % with an rms error of 0.0043 %. Counted from the instant of unloading rather than from the first resolved point, the measured recovery includes a fast component that precedes that point. The measured recovery then exceeds the model by a median of 0.011 %, with a range of −0.002 to 0.018 % over the twelve tests.

The law overpredicts the fixed-strain reaction (Fig. 3b). The rms error over the eight-hour comparison is 4.17 MPa. Over the common window, the law gives 1.29 times the measured rise from 60 s to six hours and reaches half of it in 0.42 of the measured time. On the CART record at zero stress the corresponding ratios are 1.01 and 1.08.

The two uniaxial records depart from the law in opposite directions during the first 300 s. The strain record has recovered 55 % of its eight-hour total against 40 % for the law. The stress record has reached 37 % of its eight-hour rise against 44 % for the law. Over the common

window of Fig. 3d, the law places the fixed-strain and zero-stress half-times at 1163 and 1213 s, a ratio of 0.96 against the measured 2.5. The same comparison from 300 s to eight hours is in Section S14. In the law the two constraints differ chiefly through the factor $(E + H)/H$ of Section 4.3, which makes recovery at fixed strain the faster of the two, whereas the records show it 2.5 times the slower.

5. Comparison with viscoelastic and threshold models

The uniaxial records are therefore set against two alternative forms of the recoverable branch, a viscoelastic spectrum and a threshold. The viscoelastic spectrum takes the place of the recoverable branch, while the permanent branch keeps the form of Eq. (3). The spectrum consists of positive Kelvin modes with strains $\varepsilon_{a,k}$, amplitudes J_k and retardation times τ_k, satisfying

$$\dot{\varepsilon}_{a,k} = (J_k\sigma - \varepsilon_{a,k})/\tau_k, \qquad J_k \geq 0. \tag{9}$$

One spectrum has six fixed retardation times spanning 1 to 10^5 s. A second spectrum uses twelve logarithmically spaced times from 0.1 to 10^6 s to test the sensitivity to the spectral window. All fits use the same 204 CART residuals, $\tau_v = 10$ s and $0 \leq p \leq 3$.

With its own permanent branch, each Kelvin spectrum fits both uniaxial records better than the law (Table 4, Figs. S15 and S5). The CART objectives are 1.881 and 1.685 against 1.951, and the CABT errors 4.15 and 4.03 MPa against 4.17 MPa. On the common window of Fig. 3d, the spectra place the fixed-strain and zero-stress half-times at 911 and 1241 s for six modes and 872 and 1228 s for twelve. The ratios of 0.73 and 0.71 lie further from the measured 2.5 than the 0.96 of the law. Both spectra place their largest amplitude at the longest retardation time, 10^5 or 10^6 s. Such a mode develops almost linearly during an eight-hour hold. In six hours it recovers only 19 % (at 10^5 s) or 2 % (at 10^6 s) of its strain. The slowest mode therefore acts largely as a second permanent strain over the observation window. Restricted to retardation times of 10^4 s and below, the spectra lose that mode and their advantage together. Each recoverable branch therefore assigns different fractions of the inelastic strain to slowly recoverable and permanent components.

Table 4: Controlled comparison of recoverable branches. Rows 1–3 fit all coefficients to the same 204 CART residuals. Rows 4–6 hold the permanent branch at the values identified with the other law and re-identify the recoverable branch only. The last two columns are means of per-test rms errors over the eight 5 and 8 mm bars, in percentage points of normalised hold load and of nominal unloading excursion. Coefficient counts include amplitudes that reach zero.

recoverable branch	permanent branch	coefficients	CART objective	CABT rms (MPa)	hold rms	recovery rms
back-stress branch	own fit, $B_v = 0.0288$	6	1.951	4.17	3.84	0.89
six Kelvin modes	own fit, $B_v = 0.0436$	9	1.881	4.15	4.55	1.11
twelve Kelvin modes	own fit, $B_v = 0.0465$	15	1.685	4.03	4.53	1.04
six Kelvin modes	back-stress values	6	3.367	5.19	3.83	1.06
twelve Kelvin modes	back-stress values	12	3.306	5.25	3.79	1.00
back-stress branch	six-mode values	3	11.42	1.21	5.57	1.65

The threshold alternative comes from the law of Yang (2026), which adds a time-evolving threshold to the flow and dynamic recovery to the back stress. With both removed it reduces to the back-stress element of Fig. 4 (Section S8). The threshold law takes the eight-hour reaction as the back stress at the end of the hold, whereas here that reaction is a stage of a continuing recovery (Section 4.3). A threshold above the reverse drive leaves the zero-stress record unexplained.

The role of a threshold is tested by replacing the drive $\sigma - \sigma_b$ of the recoverable branch by $\mathrm{sgn}(\sigma - \sigma_b)\langle|\sigma - \sigma_b| - Y\rangle$, with a fixed dead band $Y \geq 0$ on both directions of flow, where $\langle z\rangle = \max(z, 0)$. All six free parameters are re-identified at each Y. The CART objectives for $Y = 0$, 5, 10 and 20 MPa are 1.951, 1.951, 1.953 and 2.013, and the CABT errors 4.17, 4.12, 4.00 and 3.46 MPa. At 40 and 80 MPa the CART objective rises to 3.16 and 42.5, while the CABT errors are 1.40 and 11.83 MPa (Figs. S15c and S6). The two uniaxial controls therefore favour different dead bands, and the records expose a trade-off between the two controls rather than a common threshold bound.

The spectra buy their better uniaxial fit with nine and fifteen coefficients against six, and the dead band trades one control against the other. The law is therefore carried as identified into the bending analysis of Section 6, where the spectra are set against it on the bending records as well.

6. Application to three-point bending

6.1. Beam analysis

For the bending analysis, the bar is represented as an Euler–Bernoulli beam of span L, with a shear compliance and the machine compliance C_m of Section 2.4 in series. The law of Eqs. (1)–(3) is evaluated in this beam at six Gauss stations along the half-span and eight through the tension half of the thickness. The compression half is its mirror image, as the symmetric sinh kinetics permit. Since the identification set contains tension only, the symmetry is an assumption of the transfer and not a result of it. The curvature at a station x is the elastic curvature of the current load plus the inelastic curvature of the fibres (Chakrabarty, 2006),

$$K(x) = \frac{F\,x}{2EI} + K_{\mathrm{in}}(x), \qquad K_{\mathrm{in}}(x) = \frac{2b}{I}\int_0^{h/2} (\varepsilon_b + \varepsilon_v)\, y \,\mathrm{d}y. \tag{10}$$

Here, I is the second moment of area of the section, y the distance from the neutral axis and $\sigma = E\,(Ky - \varepsilon_b - \varepsilon_v)$ the fibre stress. The load follows from the recorded crosshead position $x_c(t)$ through the compliance of the beam and the rig,

$$F(t) = \max\left\{0,\ \frac{x_c(t) - \int_0^{L/2} K_{\mathrm{in}}(x)\, x \,\mathrm{d}x}{L^3/(48EI) + L/(4\kappa Gbh) + C_m}\right\}, \tag{11}$$

with the shear coefficient $\kappa = 5/6$ (Gere and Timoshenko, 1991) and the shear modulus $G = E/[2(1 + \nu)]$ at Poisson's ratio $\nu = 0.33$. The recorded crosshead drives the hold, and Gauss quadrature convergence is reported in Section S13.

The eleven tests are calculated with the six constants in the first row of Table 3. Beyond the crosshead, the bending records enter the calculation in two places only. The loading and unloading ramps supply the span and the machine compliance of Section 2.4, and the zero-load point of the unloading supplies the boundary condition of the recovery stage.

At the end of loading, the calculated peak loads of the eleven tests differ from the measured ones by −11.3 to +22.0 %, with a mean absolute error of 6.6 % (Fig. S7, Section S11). The hold error is the root mean square difference between calculated and measured $F(t)/F(0)$, in percentage points, at thirty log-spaced times through the hold, the calculated and measured histories each normalised by their own initial hold load. The recovery rms error is the same measure over the recovery hold, in percentage points of the nominal unloading excursion.

6.2. Stress relaxation

The law reproduces the form of the approximately logarithmic decline during the hold in every test, shown for test 7 in Fig. 5b. The mean hold error is 4.6 percentage points over the eleven tests and 3.8 over the eight 5 and 8 mm bars. The 3 mm bars are treated separately in Section 6.4. For the five 5 and 8 mm bars above 250 MPa, the mean is 3.2 percentage points. Leave-one-stress-out (LOSO) refits, each omitting one CART history, move the mean over the 5 and 8 mm bars to 3.1 to 4.2 percentage points (Section S2).

The eight-hour relaxation has systematic discrepancies at both ends of the stress range (Fig. 5c). At low nominal surface stress, 95–175 MPa, tests 1, 4, 5 and 9 relax by 20.6–32.7 % where the law gives 14–18 %. At the highest surface stresses, 421–442 MPa, tests 3, 8 and 11 relax by 31.9–35.8 % where the law gives 39–40 %. A straight line through the records loses 0.024 of the retained load per 100 MPa of surface stress, against 0.077 for the law at the same tests. Beyond its identification range the law therefore extrapolates a stress sensitivity of the hold about three times that of the bars.

6.3. Load recovery

At the recorded endpoint the model retains a positive force or has lost contact, because its inelastic deflection differs from the bar's by the amount visible in the relaxation residual. To reproduce the test boundary condition, a shift u_s is applied linearly over the unloading ramp. The shift is adjusted, with the ramp reintegrated at each trial, until the signed reaction at the ramp endpoint is zero (Section S13). The corrected endpoint is held throughout the recovery. The shift lies between −0.24 and 0.55 mm and equals in every test the difference between the recorded permanent deflection and the inelastic deflection of the law at release (Table S1). Relative to the unloading excursion $\delta_0 - \delta_1$ it is 3 to 47 % over the eleven tests and 3 to 26 % for the 5 and 8 mm bars. Since the ramp is reintegrated with the shift, the back stress and the residual stress at lift-off are those of the shifted ramp. The conditioning therefore sets the state

at the start of recovery and not only the force at the endpoint. It is still conditioned on the observed zero-load event and on no part of the recovery curve. Moving the stage instants by one second and re-conditioning lets the law lift off before the recorded stop (Table S8). The six-hour ratio of test 9 then falls from 1.65 to 0.24, so the amplitude is sensitive to the event on which the calculation is conditioned.

The six-hour ratio, the six-hour load rise of the conditioned calculation over the measured one, is 0.81 to 1.65 over the eleven tests (Fig. 6b, Table S1). The ratios are 1.22, 1.00 and 1.07 for tests 7, 8 and 11. For the 5 and 8 mm bars, the ratio generally decreases with surface stress. The law is also slow, with half-times 1.3 to 3.5 times the measured ones in every test (Figs. 3e and 6c, Table S7). The calculated rises flatten less rapidly than the measured ones. Run after an eight-hour hold over the stresses of the bars, the law places the half-time at fixed deflection at 1.5 to 3.2 times that at zero stress (Fig. 3e). The seven bars held above 250 MPa measure 0.56 to 1.26 times the zero-stress value of Section 3. At fixed strain the same law is too fast, so the error in time scale changes sign between the two constrained controls.

For the eight 5 and 8 mm bars the one-hour ratio is 0.85–1.17, all within 20 % of unity. The six-hour ratio is 1.00–1.65, with only two bars within 20 %. The ratio grows through the recovery hold in every bar but test 1 (Fig. 6a,b), so the slower calculated time scale of Fig. 3e appears in the amplitude. Judged by a band of 20 % about unity, the amplitude therefore transfers at one hour but not at six hours. The six-hour excess is largest, 1.53 to 1.65, in tests 4, 5, 9 and 10. Suppressing permanent flow during recovery changes the calculated six-hour rise by 0.5 to 1.1 % in every bar. The excess therefore lies in the recoverable branch rather than in permanent flow during the recovery hold.

The ranges in Fig. 6 give the sensitivity of the ratios to evaluation choices varied one at a time. The choices are the CART history left out, the baseline and endpoint conventions, the span and machine compliance, and a load drift of 2 N over six hours. The conventions are the instant and the load from which the rise is counted, and the drift exceeds the record noise u of Table 2. The endpoints of each range and the choice that sets it are listed in Table S11 (Section S2). At one hour the ranges include unity in eight of the eleven tests, and at six hours the smallest ratio under any of these choices is 0.76, in test 3 under the drift. The assumed drift is 30 % of the measured rise of test 1 and 14 % of that of test 4, against 1.5 to 10 % in the other nine tests. The ratios of those two tests are therefore the least secure. No half-time range in Fig. 6c reaches unity, so the calculated recovery is slower than the measured one under every choice.

In the section model the load recovery is the backflow of the back-stress element, driven by the back stress and the residual stress together (Fig. 7, Fig. S17). While contact is maintained at fixed crosshead, compatibility gives $\Delta F = -\Delta\delta_{\mathrm{in}}/C$, so the load rises as the inelastic deflection $\delta_{\mathrm{in}} = \int_0^{L/2} K_{\mathrm{in}}(x)\, x\, \mathrm{d}x$ falls, with C the denominator of Eq. (11). In test 7 the drive on the back-stress element is largest at the end of loading, in the outer fibres at midspan where the bending moment is largest. Over the eight-hour hold the outer-fibre stress at midspan relaxes from 341 to 177 MPa while the back stress there rises to 200 MPa. The drive near the faces has

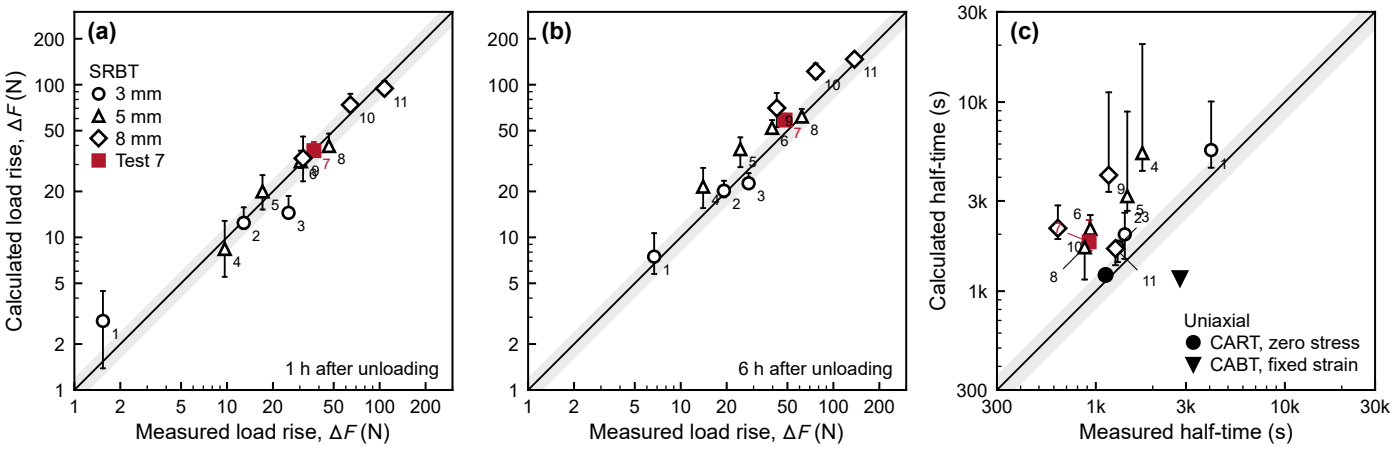


Figure 6: Calculated against measured recovery for the eleven bending tests and for the two uniaxial controls at 162.5 MPa. (a) Load rise from 60 s after unloading to one hour and (b) to six hours, on the same axes, and (c) the recovery half-time. Open symbols are the bending tests by thickness, numbered by test with test 7 in red, and filled symbols the uniaxial controls. The solid line marks equality and the grey band ±20 %. Bars are ranges under one change at a time. The changes are the leave-one-stress-out refits, the baseline and endpoint conventions, the span and machine compliance and, for the load rise, a drift of 2 N over six hours. Their endpoints are listed in Table S11.

therefore fallen to −23 MPa before unloading. In the seconds of unloading the back stress falls to 115 MPa. At lift-off the outer fibre carries a residual stress of −54 MPa, so the drive on it reaches −169 MPa, with the residual stress and the back stress acting in the same direction. Six hours later the back stress there has passed through zero to −16 MPa and the drive has fallen to −17 MPa, as in test 8 (Fig. S16).

6.4. Effect of thickness

Driven by the same backflow, the six-hour load rise, normalised by the nominal unloading excursion, falls with thickness at matched stress, and the law follows the same direction (Fig. S9a). At the matched stresses of tests 8 and 11 the 5 and 8 mm bars give measured values of 7.6 and 6.7 % where the law gives 7.6 and 7.1 %. The 3 mm bars have hold errors of 5.3 to 7.2 percentage points, against a mean of 3.8 for the 5 and 8 mm bars.

The 3 mm bars reach $\delta_0/h = 0.67$, 1.8 and 2.6. A finite-rotation calculation with frictionless rollers changes their hold errors by at most 0.25 percentage points and their recovered loads by less than 0.1 % (Section S13). Rotation therefore does not account for the larger hold errors of the thin bars, whose loading ramps show the largest toes (Section S7).

6.5. Alternative branches in bending

With the 3 mm bars set aside, the Kelvin spectra of Section 5 are run through the same beam and conditioning. The spectra also predict a monotonic rise of the recovered load through six hours. The mean hold error is 3.84 percentage points for the law against 4.55 and 4.53 for the spectra. The ordering reverses with load, the spectra giving smaller errors for the three tests

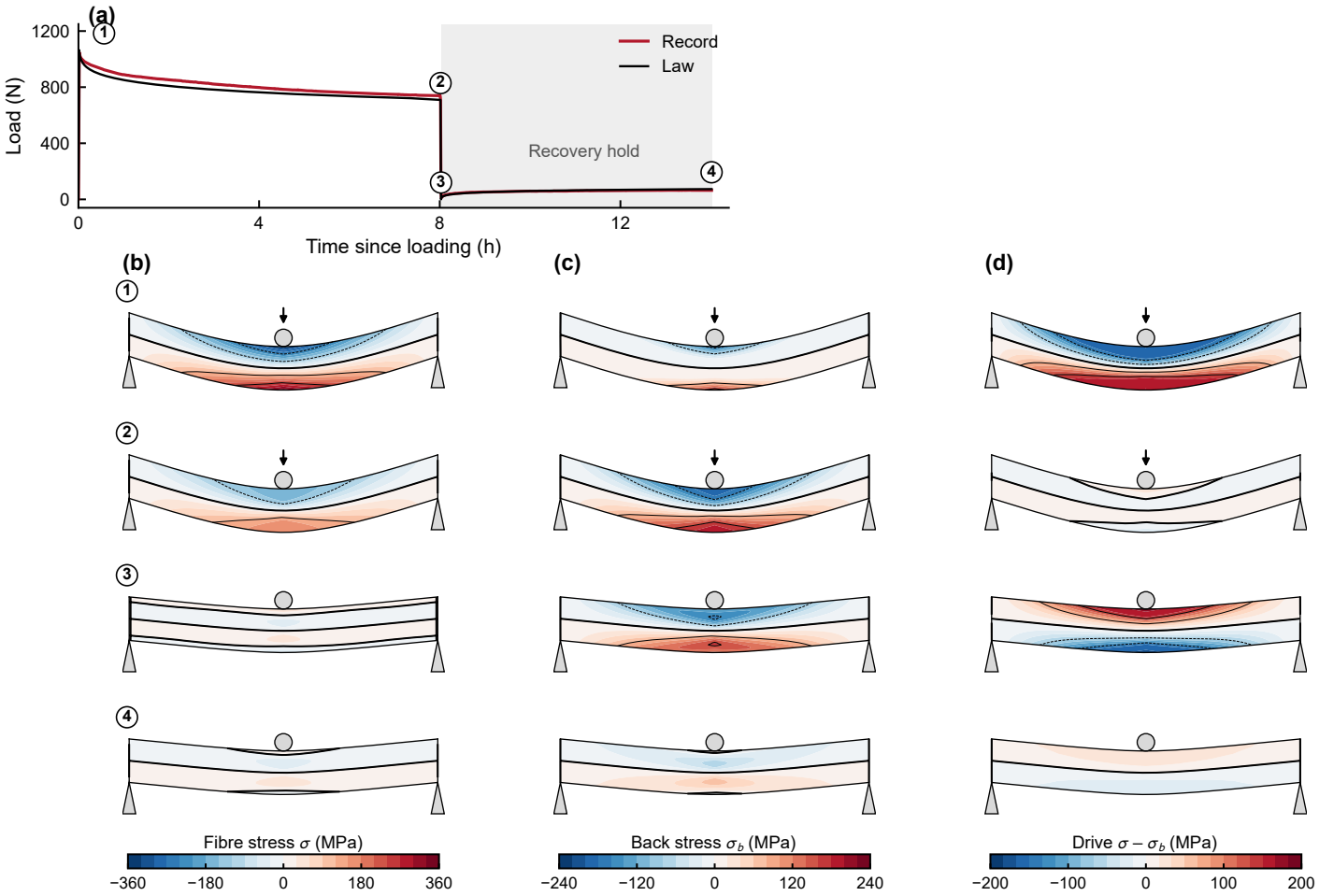


Figure 7: Calculated fields in the bent bar of test 7 (5 mm, 360 MPa) at the four instants marked on (a) the measured and calculated load. (b) Fibre stress, (c) back stress and (d) drive $\sigma - \sigma_b$ on the back-stress element over the full span, with tension on the lower face. Thin contours are drawn at every fourth colour level, dashed where the field is negative, and the heavy contour marks zero. Thickness and deflection are drawn at four times their scale, and the fields of the CART-only law are evaluated at 12 stations along the half-span and 16 through the half-thickness.

below 200 MPa, 3.4 and 3.2 against 4.8. For the five tests above 250 MPa, the spectra give larger errors, 5.2 and 5.4 against 3.2. The more stress-sensitive permanent branch of the spectra over-relaxes the surface fibres at the highest surface stresses, where the law already over-relaxes them (Section 6.2).

With a common permanent branch, the three recoverable branches give nearly the same hold error, 3.84, 3.83 and 3.79 percentage points (rows 1, 4 and 5 of Table 4). The common branch is that of the law, which then fits the uniaxial records better than either spectrum. The recovery rms errors of the spectra change by less than 5 % from their own-branch values, so for the spectra that measure is set by the recoverable branch. Conversely, the back-stress branch refitted in A_b, B_b and H on the six-mode permanent branch lowers the CABT error from 4.17 to 1.21 MPa (last row of Table 4). The CART objective then rises from 1.95 to 11.4 and the mean hold error from 3.84 to 5.57 percentage points, so the records do not support that exchange.

The timing of the recovery separates the branches more clearly than its amplitude. Over the

eight 5 and 8 mm bars the measured half-times lie between 630 and 1762 s, and the law gives 1679–5369 s, with factors above three in tests 4, 9 and 10. The six-mode spectrum with its own permanent branch gives 1007–1114 s, within a factor of 1.8 of each of the eight records. The measured half-time lengthens at low load, to 1762 s in test 4, and the law lengthens it further, to 3179–5369 s in tests 4, 5 and 9. The six-mode spectrum stays between 1007 and 1114 s at every load, so the law has the direction of the load dependence and the spectrum has none (Figs. 3e and S15b).

7. Hold duration and sensitivity of the constants

Since the half-time of the law exceeds the measured one in every bar and under every choice of Fig. 6, the question is whether the fault lies in the constants or in the form of the law. The shorter holds test the form first, and the uniaxial records then show how closely they fix each constant.

7.1. Effect of hold duration

After CART holds of 2, 4, 6 and 8 hours the recovered strain shows no sustained increase beyond four hours, whereas the law rises at every step (Fig. 8). The law and the dislocation-density model of Yang (2017) are both run without refitting. The dislocation-density model describes the same alloy with 19 constants and carries its back stress on a mobile dislocation density. The objective of that model on the 204 residuals of the uniaxial identification is 147, against 1.95 for the present law (Section S8, Fig. S11). Recovery is counted from unloading to the end of each record, 6.0 to 13.3 h later. At 137.5, 150 and 162.5 MPa the recovery falls by 11 to 23 % from two to eight hours. The common six-hour window of Table 1 gives the same trend, the recovered strain falling from 0.034 to 0.031, from 0.036 to 0.026 and from 0.042 to 0.036 %. The falls of 0.003, 0.010 and 0.006 % exceed the tracing error, which is at most 0.0017 % (Section S7), but each hold duration is one traced specimen. The specimen-to-specimen scatter of the holds, 10 to 17 % of the inelastic strain (Section 2.4), is of the order of the fall. No recovery record was repeated, so the scatter of the recovered strain itself is not measured. The records therefore exclude the sustained rise of the law more securely than they fix the size or the cause of the fall. The law rises at every step, by 17 to 29 % from two to eight hours, because its back stress is still growing at the end of the hold (Table S16). The dislocation-density model changes by −6 to +10 %, because its back stress has saturated by two hours. At 137.5 and 162.5 MPa the dislocation-density model stays within 0.0061 % of the measured recovered strain.

7.2. Sensitivity of the residuals

With the form of the law thus tested, the sensitivity of the residuals measures how closely each set of records fixes the constants. The residuals of four blocks were differentiated numerically at the CART-only parameters, with a step of 1 % in each parameter. The blocks are the

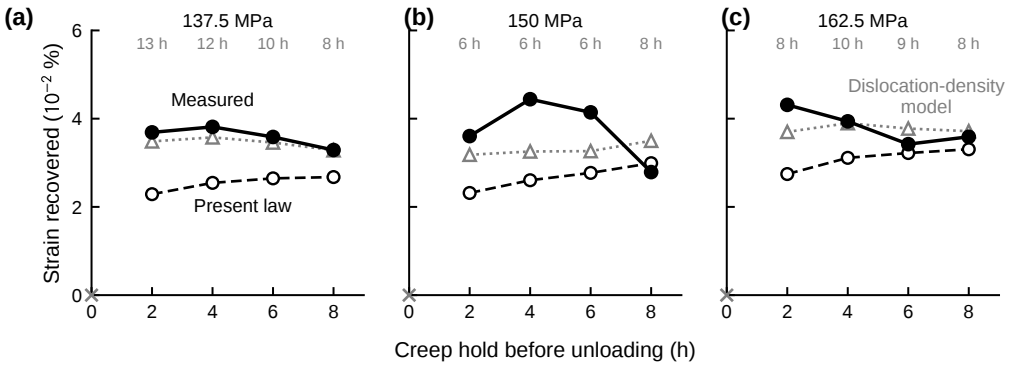


Figure 8: Strain recovered from unloading to the end of each record after CART holds of 2, 4, 6 and 8 hours at (a) 137.5, (b) 150 and (c) 162.5 MPa. Values are measured and calculated by the present law and by the dislocation-density model of Yang (2017), both without refitting. Each value uses the recovery window of its own record, whose length in hours is printed above the hold. The grey cross marks zero recovery without a hold as a reference, not a measurement.

three CART curves of the identification and the stress at fixed strain at thirty times from 300 s to eight hours. The other two blocks are the hold and recovery histories of the eight 5 and 8 mm bars, also at thirty times each. Each block is weighted by the rms of its own residual, so that the misfit of the law counts as noise. The weights are 0.0014 % in strain, 3.9 MPa in stress at its thirty sampling times, 4.3 percentage points in normalised load and 1.0 % of the nominal unloading excursion in recovered load. The inverse of the resulting information matrix gives the local scale of each parameter, relative to its value.

With the three CART curves alone, the back-stress stiffness H and sensitivity B_b have local scales of 2.9 and 2.3 %, respectively. The stress sensitivity of the permanent flow, B_v, has a local scale of 1.7 %. The prefactor A_b has a local scale of 15 % and correlations of $r = -0.87$ and 0.81 with B_b and H. The permanent-flow prefactor A_v and exponent p are correlated at $r = 0.83$, and A_v has a local scale of 16 %. The bending blocks reduce the local scale of A_b to 5.4 % and supply 36 % of its diagonal information in all four blocks.

7.3. Ranges of the constants

Beyond the local scales, the six-parameter CART identification is repeated with its input changed (Fig. S13a). One change shifts the time origin of the 162.5 MPa record by 25 s. The others take either band edge rather than the midpoint, use every second point, or omit the two pooled early hold bands. The constitutive form and parameter bounds remain fixed throughout.

Under these changes, the stiffness H and sensitivity B_b of the back-stress branch move by at most 12 and 16 %. The prefactors A_b and A_v change by factors of up to 1.4 and two, respectively, and are therefore the least closely fixed constants.

Profiles of the CART objective give the range over which each parameter can move while all the others are re-identified (Table 5, Fig. S12). The threshold is a rise of the objective by 10 % above its minimum. The sensitivities B_b and B_v and the stiffness H stay within factors of 0.93 to 1.09 of their identified values. The zero-stress recovery time $\tau_0 = 1/(A_b B_b H)$, equal

to τ_d of Eq. (4) at zero stress, is the flattest direction of the back-stress branch. The objective stays within 10 % of its minimum from 4.7 to 18.1 h and within a factor of two up to 66 h. The prefactors A_b and A_v move with τ_0, by factors of about two in either direction. The permanent-flow time τ_v is flat below 100 s (Table S4). The practical identifiability is therefore limited to the combinations that the flat directions leave fixed.

Table 5: Ranges of the identified parameters. The profile column gives the values over which the CART objective, with every other parameter re-identified, stays within 1.1 times its minimum. The LOSO column (leave one stress out) gives the three identifications on two of the three CART histories. The last two columns repeat the joint identifications of Table 3, which add three bending tests under the conventions of Section S12.

parameter	CART only	profile, ratio ≤ 1.1	LOSO	+ SRBT 3, 6, 10	+ SRBT 4, 8, 9
A_b (10^{-9} s^{-1})	1.24	0.666 to 2.49	0.906 to 2.05	2.31	2.74
B_b (MPa^{-1})	0.0591	0.0550 to 0.0613	0.0574 to 0.0595	0.0586	0.0577
H (GPa)	396.5	372.8 to 431.2	391.8 to 409.3	384.6	398.2
A_v (10^{-9} s^{-1})	6.28	2.97 to 12.5	1.54 to 8.31	2.36	3.42
B_v (MPa^{-1})	0.0288	0.0274 to 0.0307	0.0279 to 0.0300	0.0260	0.0249
p	0.408	0.318 to 0.488	0.169 to 0.449	0.186	0.214
$\tau_0 = 1/(A_b B_b H)$ (h)	9.56	4.70 to 18.1	5.97 to 13.1	5.33	4.41

The LOSO refits test the same parameters against the data rather than against the objective, each omitting one of the three CART histories and predicting it. The three refits give τ_0 of 6.0 to 13.1 h and change B_b, H and B_v by at most 4.1 %. At the objective sampling points, the held-out histories have hold-stage strain errors of 0.0023 to 0.0041 %, against 0.0013 to 0.0027 % when fitted (Table S6). Across the profiles and the refits, the zero-stress recovery time τ_0 thus remains the direction that the uniaxial records fix least.

7.4. Fitting with bending tests included

Two joint identifications therefore add bending tests 3, 6 and 10 or tests 4, 8 and 9 to the three CART histories (rows 2 and 3 of Table 3). The first set has one bar of each thickness, the second bars of 5, 5 and 8 mm.

In both joint fits the stiffness H and sensitivity B_b of the back-stress branch move much less than the prefactor A_b, which rises by a factor of about two. The stress sensitivity of the permanent flow falls by 10–14 %, from $B_v = 0.0288$ to 0.0260 and 0.0249 MPa^{-1}. The exponent p halves, and the prefactor A_v falls by a factor of 1.8 to 2.7. The permanent-flow rates of the three identifications diverge above about 200 MPa, by a factor of two at 300 MPa and three at 442 MPa. The joint identifications, which see the surface fibres of the high-load bars, give the slower flow. The bending tests outside each fit improve by one to three percentage points in eight-hour relaxation. The improved bending fit costs accuracy in the uniaxial hold-outs. The CABT error rises from 4.17 to 6.91 and 6.95 MPa, and the CART hold-out error in creep strain from 0.0019 to 0.0028 %.

The joint identifications shift several parameters relative to the uniaxial ranges in Table 5. Measured in the local scales of the CART curves (Section 7.2), the joint identifications move B_b

and H by at most 1.1. The same identifications move A_b by 4.3 and 5.5, B_v by 6.2 and 8.6 and p by −17 and −14 local scales. The stress sensitivity B_v falls below both its profile and its LOSO range, giving the slower permanent flow above 200 MPa. The zero-stress recovery time τ_0 falls to 5.3 and 4.4 h, about half its CART-only value, below the LOSO range and, in the second fit, the profile range. The exponent p falls below its profile range in both fits and A_v in the first. The constants p and A_v stay inside the LOSO range, along the correlated direction whose rate function is unchanged inside the uniaxial window. The bending records therefore add the stress sensitivity of the permanent flow at high stress and shorten the recovery time scale.

8. Free springback and die compensation

Since the bending records enter the joint fits only at the cost of larger uniaxial errors, the CART-only law at 174 °C is carried into the forming calculations. In the bending tests the deflection recovery $(\delta_1 - \delta_2)/\delta_1$ follows six hours at fixed deflection, so that it depends on the reaction developed during that constraint. The deflection recovery does not measure the free curvature of a released part. Constrained recovery and free springback are therefore computed as separate boundary-value problems.

A released part springs back freely instead of at fixed deflection, at zero external moment. The section model is reduced to pure bending to compare the two conditions. A 5 mm section is loaded instantaneously to an initial surface stress between 250 and 440 MPa. After an eight-hour hold at constant curvature or constant moment, it is either released or held at its instantaneous zero-moment curvature. The time-hardening factor $(1 + t/\tau_v)^{-p}$ of the permanent branch runs from loading through recovery. The elastic springback at release is $M_h/(EI)$, with M_h the moment at the end of the hold, and the delayed springback, the further loss of curvature at zero moment, is expressed as a fraction of it. The constrained recovery is reported as the returning moment.

Held at constant curvature, i.e. die-clamped, the section relaxes its moment to between 49 and 71 % of the initial value over eight hours (Table 6). The release being elastic, the section keeps the relaxed share of the moment as curvature, 29 to 51 % of the imposed value. Held at constant moment, the same initial surface stress produces 1.6 to 8.6 times the initial curvature, because the fibres creep forward under a load that does not relax.

For the die-clamped histories the delayed springback reaches 9 to 12 % of the elastic springback in one hour, 13 to 16 in six hours and 16 to 18 in thirty days. Over the four stresses, six hours give 83 to 87 % of the thirty-day value and one day gives 98 % (Table S19).

The residual stress at release is compressive near the surface and tensile inside (Fig. S10b), and it relaxes at zero moment. If the release curvature is held instead, the returning moment reaches 11 to 13 % of the released moment in six hours. Since the three-point bars carry a nonuniform moment, it follows that a pure-bending moment ratio cannot replace their six-hour ratio.

The die compensation needed for a target shape depends on the time at which the shape is assessed. Let the targets be the release curvatures produced by initial elastic surface stresses of 200, 300 and 400 MPa. Kept at the forming temperature, the section loses 51, 30 and 20 % of these curvatures in thirty days. Solving directly for the die curvature that retains each target gives initial stresses of 253, 345 and 444 MPa, i.e. 26, 15 and 11 % more die curvature. The curvature kept by the die-clamped section and the compensation it requires are plotted in Fig. 9.

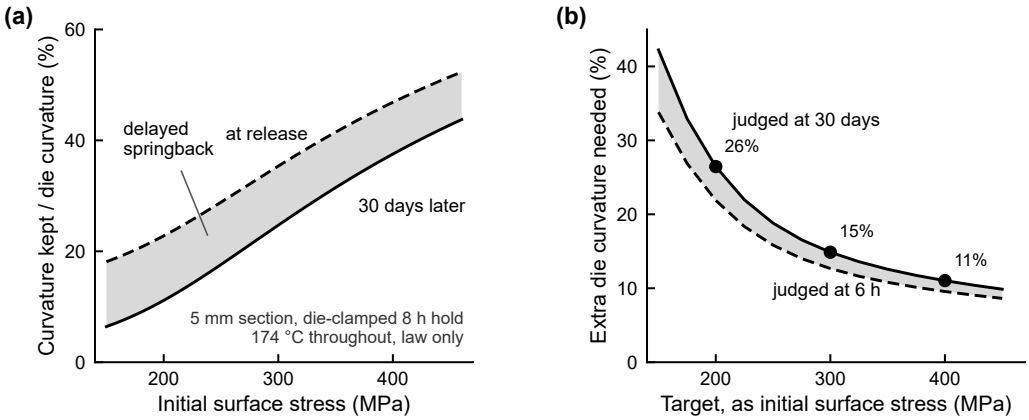


Figure 9: Die-clamped 5 mm section of Table 6 after an eight-hour hold and release, calculated at 174 °C with the constitutive parameters fixed. (a) Curvature kept at release and thirty days later, relative to the die curvature, with the delayed springback between them shaded. (b) Additional die curvature needed to keep a target release curvature, judged at six hours or at thirty days, with the three targets of the text marked. The target is named by the initial elastic surface stress whose eight-hour die-clamped hold produces that release curvature.

A continuous map between 150 and 460 MPa extends the four stresses of Table 6 (Fig. S14). The die-clamped hold keeps between 18 and 52 % of the imposed curvature at release and between 6 and 44 % after thirty days. After a hold at constant moment, the curvature retained at release passes the elastic loading curvature just above 290 MPa and reaches 7.6 times it at 440 MPa. The two holds differ in retained curvature by an order of magnitude at 440 MPa, whereas their delayed springback differs by at most four percentage points.

Assessed at thirty days, the additional die curvature falls along the map from 42 % at a target stress of 150 MPa to 10 % at 450 MPa. Assessed at six hours it falls from 34 to 9 %. The die surface stress of the compensation then reaches about 495 MPa, beyond the 442 MPa of the bending tests.

With the three LOSO refits and the two joint identifications of Table 5, whose zero-stress recovery times span 4.4 to 13.1 h, the calculation is repeated (Table S20). The six-hour delayed springback at 250 to 440 MPa then lies between 12.0 and 17.3 % and the thirty-day value between 15.3 and 18.8 %. The additional die curvature assessed at thirty days lies between 9.5 and 47 % over target stresses of 150 to 450 MPa. Relative to the CART-only set, the thirty-day compensation moves by at most 5.2 percentage points and the six-hour compensation by at most 8.8, both at the 150 MPa target. The ordering of the targets and the growth of the compensation from six hours to thirty days are the same for every set. These ranges are those of one consti-

Table 6: Pure bending of a 5 mm section at equal initial surface stress σ_{s0}, with an eight-hour hold at constant moment or at constant curvature and release to zero moment. K_0 is the elastic curvature at loading, and K_h, K_r and K_{30} the curvatures at the end of the hold, at release and thirty days later. $S(t)$ is the delayed springback as a fraction of the elastic springback at release, and σ_res the surface residual stress at release and after thirty days. The last column is the returning moment, the fraction of the released moment that returns in six hours if the curvature is held after release, as in the bending tests. The thirty-day columns and the rows at constant moment above 300 MPa extrapolate the law beyond the strains of the identification set, at constant temperature and fixed constitutive parameters.

held	σ_{s0} (MPa)	K_h/K_0	K_r/K_0	K_{30}/K_0	$S_{1\,\mathrm{h}}$ (%)	$S_{6\,\mathrm{h}}$ (%)	$S_{24\,\mathrm{h}}$ (%)	$S_{30\,\mathrm{d}}$ (%)	σ_res (MPa) release / 30 d	M back 6 h (%)
curvature	250	1.00	0.29	0.18	9	13	15	16	−27 / −19	11
curvature	300	1.00	0.35	0.25	10	14	16	16	−38 / −27	12
curvature	360	1.00	0.43	0.33	11	15	17	17	−48 / −34	13
curvature	440	1.00	0.51	0.42	12	16	17	18	−56 / −39	13
moment	250	1.62	0.62	0.47	10	13	15	15	−52 / −36	11
moment	300	2.12	1.12	0.96	11	14	15	15	−75 / −49	12
moment	360	3.41	2.41	2.26	12	14	15	15	−100 / −58	12
moment	440	8.60	7.60	7.46	13	14	15	14	−128 / −63	12

tutive form. The Kelvin spectra of Section 5 place their largest amplitude at retardation times of 10^5 to 10^6 s, which six hours of record do not resolve and which thirty days would. The thirty-day values are therefore projections of the law beyond the window of the records, and the compensation they imply is conditional on its form.

9. Discussion

Carried into die compensation, the CART-only law recovers too slowly in bending, and its CART recovery grows with hold duration whereas the records show no sustained increase beyond four hours. Both errors bear on the questions set at the outset, i.e. how much relaxed strain returns, how fast and under which constraint. For either error, the question is whether the fault lies in the constants or in the form of the law. The two errors are examined first, then their consequence for constitutive modelling, and last a microstructural reading of the back-stress stiffness and of its dependence on hold time.

9.1. The two systematic errors

The constants can shorten the recovery time in bending, but only at a cost in the uniaxial fit. With three bending tests included, the joint identifications of Section 7.4 raise A_b by a factor of about two, at the cost of CABT errors of 6.9 MPa. The forming calculations give a six-hour delayed springback of 16 to 17 % with the two joint sets, rather than 13 to 16 with the CART-only set.

The second error, with hold duration, arises because the back stress of the law is still growing at the end of an eight-hour hold (Section 7.1). The dislocation-density model of that section, whose back stress saturates within two hours, follows the measured trend but gives 75 times the objective of the law on the uniaxial residuals. The law contains no stiffening of the recoverable element as the alloy ages. A stiffness H that rises during the hold reduces the error with hold duration. A falling mobile dislocation density would produce such stiffening through the bowing

of pinned segments (Section 9.3). Stress rebound during relaxation-ageing of AA7050 under elastic loading has also been attributed to evolving dislocation structure (Zhang et al., 2025). The uniaxial records admit a small stiffening. A variant with $H = H_0(1 + t/3600\,\mathrm{s})^q$, refitted on the same residuals, gives $q = 0.22$ and lowers the CART objective by 4 %. The predicted increase in recovered strain from two to eight hours falls to 7–20 %, without reversing the trend. The bending half-times remain unchanged, while the CABT error rises to 5.2 MPa. The first error therefore lies partly in the constants, and the second, if the fall is not specimen variation, in the form of the law.

9.2. Implications for constitutive modelling

Both errors lie in the response after unloading, while creep-ageing models are identified on forward creep or stress relaxation (Ho et al., 2004a; Li et al., 2017b; Rong et al., 2021; Zhang et al., 2013; Zheng et al., 2018) and are used to predict a shape after unloading. The present records show that the response after unloading is a separate test, and one that a model passes or fails independently of its forward fit. Two conditions apply to a yield-type threshold on the reverse flow. First, it permits recovery only while the back stress left at unloading exceeds its dead band. Second, the two uniaxial controls favour different dead bands (Section 5). A creep-ageing model whose ageing threshold exceeds the back stress at unloading recovers nothing.

The permanent branch limits transfer of the bending-hold response more than the recoverable branch does. One sinh stress sensitivity identified between 137.5 and 162.5 MPa over-relaxes the surface fibres at the highest stresses of the bending tests (Section 6.2). That attribution rests on the symmetric kinetics of Section 6.1. An asymmetry between tension and compression creep would enter the same fibres, and the bending records cannot separate the two. The joint identifications reduce the over-relaxation but pay for it in the uniaxial fit. Extending the branch needs uniaxial records at higher stress and in compression. It also needs histories that separate ageing from stress dependence, of the kind reported for anisotropic creep-ageing and multi-step relaxation (Wang et al., 2024; Zhou et al., 2026).

9.3. Microstructural interpretation

The recoverable branch carries a back-stress stiffness $H = 397$ GPa, six times E, and the back stress reaches nine tenths of the applied stress by the end of an eight-hour hold. Fribourg et al. (2011) measured internal stresses of 50–200 MPa in reverse-loading tests on AA7449, rising with forward strain and levelling off near a plastic strain of 0.02 to 0.03. The authors judged the range too high for stored Orowan loops alone, for which they expected 10–50 MPa. The excess was attributed to glide that is partly reversible, in which mobile dislocations return along the path they came by. The back stress of 122–147 MPa identified here is of the same order, and the recoverable strain plays the part of the reversible glide in that account.

The simplest reservoir of such strain is a population of mobile segments of length ℓ pinned at both ends by precipitates. Each segment bows against the line tension $Gb_\mathrm{v}^2/2$, with b_v the Burgers vector (Hull and Bacon, 2011). In the small-bow limit, a density ρ_m of such line bowing

under a resolved shear stress τ produces the shear strain $\rho_m \ell^2 \tau/(6G)$ (Gibeling and Nix, 1981). Converted to tension with the Taylor factor $M_T = 3.06$, the stiffness of the reservoir is

$$H = \frac{\sigma_b}{\varepsilon_b} = \frac{6M_T^2 G}{\rho_m \ell^2}. \tag{12}$$

The identified H and the shear modulus $G = E/[2(1+\nu)] = 24.5\,\mathrm{GPa}$ require $\rho_m \ell^2 = 3.5$, so that ℓ is 1.9 times the mean spacing $\rho_m^{-1/2}$ of the mobile line. A segment cannot carry more than the Orowan stress $\tau = Gb_\mathrm{v}/\ell$ (Hull and Bacon, 2011). For $\sigma_b = 147\,\mathrm{MPa}$, i.e. $\tau = 48\,\mathrm{MPa}$, and $b_\mathrm{v} = 0.286\,\mathrm{nm}$, the Orowan bound gives, to order of magnitude, $\ell \leq 146\,\mathrm{nm}$ and therefore $\rho_m \geq 1.6 \times 10^{14}\,\mathrm{m}^{-2}$.

Since H in Eq. (12) rises as ρ_m falls at fixed segment length, a decrease in mobile dislocation density during the hold is a candidate for the error with hold duration. Li et al. (2019a) describe two stages in the creep-ageing of an Al–Zn–Mg–Cu alloy, in the first of which tangling and pile-up hinder the dislocations and the mobile dislocation density falls. The yield strength of AA7050 crept at 162.5 MPa falls from 493 to 462 MPa between 4 and 8 h (Yang et al., 2023), so the obstacle structure still evolves over that interval. Relaxation of AA7075 at 150 °C, on the other hand, has been reported with only a limited loss of mobile dislocation density (Nguyen et al., 2026). Multi-step relaxation-ageing of AA7050 also shows a path-dependent microstructural evolution (Zhou et al., 2026). The measurement that would decide between them is a mobile dislocation density tracked through the hold.

10. Conclusions

1. The stress-relaxation and back-stress bending test records the load that returns at fixed deflection after a creep relaxation hold and unloading. It adds a third condition of constraint to recovery at zero stress and at fixed strain, and a law identified under one condition can be checked under the other two without refitting.
2. The CART-only back-stress law describes important features of recovery under three conditions of constraint, but its transfer from one condition to another is incomplete. The fixed-strain stress recovery has an rms error of 4.17 MPa. In eleven bending tests, the mean hold error is 4.6 percentage points, or 3.8 for the 5 and 8 mm bars. With unloading conditioned on the observed zero-load point, the calculated one-hour load rises lie within 20 % of the measured values for the 5 and 8 mm bars. Over all eleven tests the six-hour rises are 0.81 to 1.65 times the measured values (1.00 to 1.65 for the 5 and 8 mm bars). The bending half-times are 1.3 to 3.5 times the measured ones, whereas at fixed strain the law reaches half of its six-hour rise in 0.42 of the measured time. The error in time scale therefore changes sign between the two constrained controls. The law also predicts recovered strain that keeps increasing with hold duration where the CART records show no sustained increase beyond four hours.

3. The records constrain the law without selecting a unique recovery mechanism. Positive Kelvin spectra and the back-stress branch give nearly the same hold error when they share the permanent branch. A dead band of 40 MPa reduces the fixed-strain error while worsening the CART objective, so the two uniaxial controls favour different dead bands. Profiles of the CART objective hold the back-stress stiffness and the two stress sensitivities within factors of 0.93 to 1.09, whereas the zero-stress recovery time spans 4.7 to 18.1 h. The bending records add constraints on the permanent-flow stress sensitivity above about 200 MPa and on the recovery time scale.
4. Free springback occurs at zero external moment rather than at fixed deflection, where constrained recovery develops a reaction. For a die-clamped 5 mm section at 250–440 MPa, the law projects a delayed springback at the forming temperature of 13 to 16 % of the elastic springback in six hours. After thirty days the fraction reaches 16 to 18 %. Across target surface stresses of 150–450 MPa, retaining the thirty-day target curvature requires 10 to 42 % more die curvature than compensation at release. The three leave-one-stress-out refits and the two joint identifications move the thirty-day compensation by at most 5.2 percentage points without changing the ordering of the targets. The projection is conditional on the form of the law, which the records test to six hours only.

Recovery after unloading therefore provides a separate test for a constitutive law that is to predict the retained shape of a formed part.

Declarations

Funding

Support was provided by the National Science and Technology Council, Taiwan, under grant 115-2221-E-027-065-MY2.

Competing interests

The author has no relevant financial or non-financial interests to disclose.

Author contributions

Yo-Lun Yang is the sole author and carried out the conceptualisation, experiments, analysis and writing.

Data availability

The records, identification inputs, parameters, analysis code and figure code that support this study are available from the corresponding author on reasonable request.

References

Zaloa Arechabaleta, Peter van Liempt, and Jilt Sietsma. Quantification of dislocation structures from anelastic deformation behaviour. *Acta Materialia*, 115:314–323, 2016. doi: 10.1016/j.actamat.2016.05.040.

P. J. Armstrong and C. O. Frederick. A mathematical representation of the multiaxial Bauschinger effect. Technical Report RD/B/N731, Central Electricity Generating Board, 1966. Reprinted in Materials at High Temperatures 24 (2007) 1–26.

ASTM International. ASTM E328-21: Standard test methods for stress relaxation for materials and structures. Technical report, ASTM International, West Conshohocken, PA, 2021.

Başaran Bekir Başpınar, Mehmet Fatih Aycan, and İbrahim Uslan. Investigation of springback behavior in creep age forming of AA2024 sheets used in the aerospace industry. *International Journal of Material Forming*, 19(2):45, 2026. doi: 10.1007/s12289-026-02011-z.

J. J. Bhattacharyya, B. Bittmann, and S. R. Agnew. The effect of precipitate-induced back-stresses on plastic anisotropy: Demonstrated by modeling the behavior of aluminum alloy, 7085. *International Journal of Plasticity*, 117:3–20, 2019. doi: 10.1016/j.ijplas.2018.04.011.

T. J. Bian, H. Li, J. C. Yang, C. Lei, C. H. Wu, L. W. Zhang, and G. Y. Chen. Through-thickness heterogeneity and in-plane anisotropy in creep aging of 7050 Al alloy. *Materials & Design*, 196:109190, 2020. doi: 10.1016/j.matdes.2020.109190.

S. R. Bodner and Y. Partom. Constitutive equations for elastic-viscoplastic strain-hardening materials. *Journal of Applied Mechanics*, 42(2):385–389, 1975. doi: 10.1115/1.3423586.

J.-L. Chaboche. Cyclic viscoplastic constitutive equations, part I: a thermodynamically consistent formulation. *Journal of Applied Mechanics*, 60(4):813–821, 1993. doi: 10.1115/1.2900988.

J. L. Chaboche. A review of some plasticity and viscoplasticity constitutive theories. *International Journal of Plasticity*, 24:1642–1693, 2008. doi: 10.1016/j.ijplas.2008.03.009.

J. Chakrabarty. *Theory of Plasticity*. Butterworth-Heinemann, Oxford, 3rd edition, 2006. doi: 10.1016/C2009-0-05774-2.

A. H. Cottrell. The time laws of creep. *Journal of the Mechanics and Physics of Solids*, 1:53–63, 1952. doi: 10.1016/0022-5096(52)90006-9.

Jay Christian Dandrea and Roderic Lakes. Creep and creep recovery of cast aluminum alloys. *Mechanics of Time-Dependent Materials*, 13(4):303–315, 2009. doi: 10.1007/s11043-009-9089-6.

Sowmya Daroju, Toshihiko Kuwabara, Rishabh Sharma, David T. Fullwood, Michael P. Miles, and Marko Knezevic. Experimental characterization and crystal plasticity modeling for predicting load reversals in AA6016-T4 and AA7021-T79. *International Journal of Plasticity*, 153:103292, 2022. doi: 10.1016/j.ijplas.2022.103292.

Alan D. Freed and Kevin P. Walker. Viscoplasticity with creep and plasticity bounds. *International Journal of Plasticity*, 9(2):213–242, 1993. doi: 10.1016/0749-6419(93)90030-T.

G. Fribourg, Y. Bréchet, A. Deschamps, and A. Simar. Microstructure-based modelling of isotropic and kinematic strain hardening in a precipitation-hardened aluminium alloy. *Acta Materialia*, 59(9):3621–3635, 2011. doi: 10.1016/j.actamat.2011.02.035.

F. Garofalo. *Fundamentals of Creep and Creep-Rupture in Metals*. Macmillan, New York, 1965.

J. M. Gere and S. P. Timoshenko. *Mechanics of Materials*. Springer, Boston, MA, 3rd edition, 1991. doi: 10.1007/978-1-4899-3124-5.

P. Germain, Q. S. Nguyen, and P. Suquet. Continuum thermodynamics. *Journal of Applied Mechanics*, 50(4b):1010–1020, 1983. doi: 10.1115/1.3167184.

J. C. Gibeling and W. D. Nix. Observations of anelastic backflow following stress reductions during creep of pure metals. *Acta Metallurgica*, 29:1769–1784, 1981. doi: 10.1016/0001-6160(81)90010-9.

B. Halphen and Q. S. Nguyen. Sur les matériaux standard généralisés. *Journal de Mécanique*, 14:39–63, 1975.

Takayuki Hama, Tomotaka Suzuki, Yuya Nakatsuji, Takeyuki Sakai, and Hirohiko Takuda. Time-dependent springback of various sheet metals: An experimental study. *Materials Transactions*, 61(5):941–947, 2020. doi: 10.2320/matertrans.MT-M2019283.

E. W. Hart. Constitutive relations for the nonelastic deformation of metals. *Journal of Engineering Materials and Technology*, 98:193–202, 1976. doi: 10.1115/1.3443368.

K. C. Ho, J. Lin, and T. A. Dean. Constitutive modelling of primary creep for age forming an aluminium alloy. *Journal of Materials Processing Technology*, 153–154:122–127, 2004a. doi: 10.1016/j.jmatprotec.2004.04.304.

K. C. Ho, J. Lin, and T. A. Dean. Modelling of springback in creep forming thick aluminum sheets. *International Journal of Plasticity*, 20:733–751, 2004b. doi: 10.1016/S0749-6419(03)00078-0.

D. Hull and D. J. Bacon. *Introduction to Dislocations*. Butterworth-Heinemann, Oxford, 5th edition, 2011. doi: 10.1016/C2009-0-64358-0.

P.-P. Jeunechamps, K. C. Ho, J. Lin, J.-P. Ponthot, and T. A. Dean. A closed form technique to predict springback in creep age-forming. *International Journal of Mechanical Sciences*, 48 (6):621–629, 2006. doi: 10.1016/j.ijmecsci.2006.01.005.

E. Krempl. Rate (time)-dependent deformation behavior: an overview of some properties of metals and solid polymers. *International Journal of Plasticity*, 19(7):1069–1095, 2003. doi: 10.1016/S0749-6419(03)00002-0.

Aaron C. L. Lam, Zhusheng Shi, Jianguo Lin, and Xia Huang. Influences of residual stresses and initial distortion on springback prediction of 7B04-T651 aluminium plates in creep-age forming. *International Journal of Mechanical Sciences*, 103:115–126, 2015a. doi: 10.1016/j.ijmecsci.2015.09.004.

Aaron C.L. Lam, Zhusheng Shi, Haoliang Yang, Li Wan, Catrin M. Davies, Jianguo Lin, and Shijie Zhou. Creep-age forming aa2219 plates with different stiffener designs and pre-form age conditions: Experimental and finite element studies. *Journal of Materials Processing Technology*, 219:155–163, 2015b. doi: 10.1016/j.jmatprotec.2014.12.012.

Shanfeng Lao, Lihua Zhan, Wei Qian, Yongqian Xu, Bolin Ma, Chuhui Liu, Minghui Huang, Youliang Yang, Kuigen Chen, Nanhui Peng, Tuanjie Gao, and Hongfei Xi. Creep aging behavior of a thermo-mechanical treated 7B04 aluminum alloy. *Metals*, 13(2):182, 2023. doi: 10.3390/met13020182.

K. C. Le and T. M. Tran. Thermodynamic dislocation theory: Bauschinger effect. *Physical Review E*, 97(4):043002, 2018. doi: 10.1103/PhysRevE.97.043002.

Hyongjoon Lee, Hobyung Chae, You Sub Kim, Min Ji Song, Sangyeob Lim, Kali Prasad, Hariharan Krishnaswamy, Jayant Jain, Ke An, and Soo Yeol Lee. Viscoplastic lattice strain during repeated relaxation of age-hardened Al alloy. *Mechanics of Materials*, 158:103899, 2021a. doi: 10.1016/j.mechmat.2021.103899.

Kuo-Long Lee, Bo-You Liu, and Wen-Fung Pan. Response of round-hole tubes submitted to pure bending creep and pure bending relaxation. *Advances in Mechanical Engineering*, 13 (9):16878140211049124, 2021b. doi: 10.1177/16878140211049124.

J. Lemaitre and J.-L. Chaboche. *Mechanics of Solid Materials*. Cambridge University Press, Cambridge, 1990.

Heng Li, Tian-Jun Bian, Chao Lei, Gao-Wei Zheng, and Yu-Fei Wang. Dynamic interplay between dislocations and precipitates in creep aging of an Al–Zn–Mg–Cu alloy. *Advances in Manufacturing*, 7(1):15–29, 2019a. doi: 10.1007/s40436-018-0240-y.

Y. Li, Z. Shi, Y.-L. Yang, Q. Rong, R. Said, and P. Saillard. Effects of asymmetric creep-ageing behaviour on springback of AA2050-T34 after creep age forming. In *Procedia Engineering*, volume 207, pages 287–292, 2017a. doi: 10.1016/j.proeng.2017.10.776.

Yong Li and Zhusheng Shi. A new method to characterize and model stress-relaxation aging behavior of aluminum alloys under age forming conditions. *Metallurgical and Materials Transactions A*, 53(4):1345–1360, 2022. doi: 10.1007/s11661-022-06594-5.

Yong Li, Zhusheng Shi, Jianguo Lin, Yo-Lun Yang, Qi Rong, Bo-Ming Huang, Tian-Fu Chung, Cheng-Si Tsao, Jer-Ren Yang, and Daniel S. Balint. A unified constitutive model for asymmetric tension and compression creep-ageing behaviour of naturally aged Al–Cu–Li alloy. *International Journal of Plasticity*, 89:130–149, 2017b. doi: 10.1016/j.ijplas.2016.11.007.

Yong Li, Zhusheng Shi, Jianguo Lin, Yo-Lun Yang, Patrick Saillard, and Rajab Said. FE simulation of asymmetric creep-ageing behaviour of AA2050 and its application to creep age forming. *International Journal of Mechanical Sciences*, 140:228–240, 2018a. doi: 10.1016/j.ijmecsci.2018.03.003.

Yong Li, Zhusheng Shi, Jianguo Lin, Yo-Lun Yang, Patrick Saillard, and Rajab Said. Effect of machining-induced residual stress on springback of creep age formed AA2050 plates with asymmetric creep-ageing behaviour. *International Journal of Machine Tools and Manufacture*, 132:113–122, 2018b. doi: 10.1016/j.ijmachtools.2018.05.003.

Yong Li, Qi Rong, Zhusheng Shi, Xiaoguang Sun, Lichun Meng, and Jianguo Lin. An accelerated springback compensation method for creep age forming. *The International Journal of Advanced Manufacturing Technology*, 102(1-4):121–134, 2019b. doi: 10.1007/s00170-018-3175-3.

Yong Li, Wanni Gan, Xia Huang, Ying Zhang, Wenbin Zhou, Dongsheng Li, and Yuansong Zeng. A quantitative study of machining induced residual stress and its effect on subsequent creep age forming of aluminium alloy panels. *Journal of Materials Processing Technology*, 321:118147, 2023. doi: 10.1016/j.jmatprotec.2023.118147.

H. Lim, M. G. Lee, J. H. Sung, and R. H. Wagoner. Time-dependent springback. *International Journal of Material Forming*, 1(S1):157–160, 2008. doi: 10.1007/s12289-008-0015-2.

J. Lin, K. C. Ho, and T. A. Dean. An integrated process for modelling of precipitation hardening and springback in creep age-forming. *International Journal of Machine Tools and Manufacture*, 46:1266–1270, 2006. doi: 10.1016/j.ijmachtools.2006.01.026.

Kuntao Liu, Shanglei Yang, and Jieshi Chen. A comprehensive review on creep age forming: Process parameters, alloying effects, and constitutive modeling. *Materials Science and Technology*, 42:1150–1179, 2026. doi: 10.1177/02670836251395498.

G. J. Lloyd and R. J. McElroy. On the anelastic contribution to creep. *Acta Metallurgica*, 22: 339–348, 1974. doi: 10.1016/0001-6160(74)90173-4.

Fenggong Lyu, Yong Li, Zhusheng Shi, Xia Huang, Yuansong Zeng, and Jianguo Lin. Stress and temperature dependence of stress relaxation ageing behaviour of an Al–Zn–Mg alloy. *Materials Science and Engineering: A*, 773:138859, 2020. doi: 10.1016/j.msea.2019.138859.

Francesco Mainardi and Giorgio Spada. On the viscoelastic characterization of the jeffreys–lomnitz law of creep. *Rheologica Acta*, 51:783–791, 2012. doi: 10.1007/s00397-012-0634-x.

Kouki Matsugi and Ryutaro Hino. Influence of bend holding on springback and time-dependent springback in sheet metal bending. *Materials Transactions*, 65(10):1373–1376, 2024. doi: 10.2320/matertrans.MT-P2024003.

Kouki Matsugi and Ryutaro Hino. Numerical analysis of time-dependent springback in L-Bending of advanced high-strength steel sheet based on unified constitutive model. *Materials Transactions*, 66:366–375, 2025. doi: 10.2320/matertrans.mt-p2024006.

A. Miller. An inelastic constitutive model for monotonic, cyclic, and creep deformation: Part I—equations development and analytical procedures. *Journal of Engineering Materials and Technology*, 98(2):97–105, 1976. doi: 10.1115/1.3443367.

Ole Runar Myhr, Tore Børvik, Calin D. Marioara, Sigurd Wenner, and Odd Sture Hopperstad. Nanoscale modelling of combined isotropic and kinematic hardening of 6000 series aluminium alloys. *Mechanics of Materials*, 151:103603, 2020. doi: 10.1016/j.mechmat.2020.103603.

V. C. Nardone, D. E. Matejczyk, and J. K. Tien. A model for anelastic relaxation controlled cyclic creep. *Metallurgical Transactions A*, 16(6):1117–1122, 1985. doi: 10.1007/BF02811680.

Thanh-Dat Nguyen, You Sub Kim, Byungju Lee, Soon-Ku Hong, Tien-Dung Nguyen, Hobyung Chae, Eunjoo Shin, Ke An, and Soo Yeol Lee. Elevated-temperature stress-relaxation behavior of age-hardened AA7075. *Mechanics of Materials*, 217:105650, 2026. doi: 10.1016/j.mechmat.2026.105650.

A. S. Nowick and B. S. Berry. *Anelastic Relaxation in Crystalline Solids*. Academic Press, New York, 1972.

N. Ohno and J.-D. Wang. Kinematic hardening rules with critical state of dynamic recovery, part I: formulation and basic features for ratchetting behavior. *International Journal of Plasticity*, 9:375–390, 1993. doi: 10.1016/0749-6419(93)90042-O.

P. Perzyna. Fundamental problems in viscoplasticity. *Advances in Applied Mechanics*, 9:243–377, 1966. doi: 10.1016/S0065-2156(08)70009-7.

Qi Rong, Zhusheng Shi, Yong Li, and Jianguo Lin. Constitutive modelling and its application to stress-relaxation age forming of aa6082 with elastic and plastic loadings. *Journal of Materials Processing Technology*, 295:117168, 2021. doi: 10.1016/j.jmatprotec.2021.117168.

Junjie Shen, Ken-ichi Ikeda, Satoshi Hata, and Hideharu Nakashima. Transient creep in high-purity aluminum at ultra-low strain rate and room temperature by constant stress and changing-stress experiments. *Materials Transactions*, 52(10):1885–1889, 2011. doi: 10.2320/matertrans.M2011175.

N. K. Sinha. Limitations of stress relaxation tests for determining stress dependence of strain rate at high temperatures. *Scripta Materialia*, 48:731–736, 2003. doi: 10.1016/S1359-6462(02)00535-3.

A. Torkabadi, E. S. Perdahcıoğlu, V. T. Meinders, and A. H. van den Boogaard. On the nonlinear anelastic behavior of AHSS. *International Journal of Solids and Structures*, 151:2–8, 2018. doi: 10.1016/j.ijsolstr.2017.03.009.

Ville Tulkki and Timo Ikonen. Viscoelastic modelling of Zircaloy cladding in-pile transient creep. *Journal of Nuclear Materials*, 457:324–329, 2015. doi: 10.1016/j.jnucmat.2014.11.100.

J. F. Wang, R. H. Wagoner, W. D. Carden, D. K. Matlock, and F. Barlat. Creep and anelasticity in the springback of aluminum. *International Journal of Plasticity*, 20:2209–2232, 2004. doi: 10.1016/j.ijplas.2004.05.008.

Xi Wang, Qi Rong, Zhusheng Shi, and Jianguo Lin. Improved creep behaviour for a high strength Al–Li alloy in creep age forming: Experimental studies and constitutive modelling. *International Journal of Plasticity*, 159:103447, 2022. doi: 10.1016/j.ijplas.2022.103447.

Xi Wang, Qi Rong, Zhusheng Shi, and Jianguo Lin. An efficient closed-form solution for springback prediction and compensation in elastic–plastic creep age forming. *The International Journal of Advanced Manufacturing Technology*, 125(3-4):1115–1133, 2023. doi: 10.1007/s00170-022-10607-3.

Xi Wang, Zhusheng Shi, and Jianguo Lin. A generalised framework for modelling anisotropic creep-ageing deformation and strength evolution of 2xxx aluminium alloys. *International Journal of Plasticity*, 182:104114, 2024. doi: 10.1016/j.ijplas.2024.104114.

Xi Wang, Zhusheng Shi, and Jianguo Lin. Deformation, strength and corrosion resistance evolutions of AA7475 under creep-ageing with various pre-treatments. *Materials Science and Engineering: A*, 948:149278, 2025. doi: 10.1016/j.msea.2025.149278.

Ling-zhi Xu, Can-yu Tong, Chang-zhi Liu, Li-hua Zhan, Ming-hui Huang, You-liang Yang, Dong-yang Yan, Jian-hua Yin, Hui Xia, and Yong-qian Xu. A novel constitutive model for two-stage creep aging process of 7B50 aluminum alloy and its application in springback prediction. *Transactions of Nonferrous Metals Society of China*, 35(3):734–748, 2025. doi: 10.1016/S1003-6326(24)66711-7.

Jianshi Yang, Chunhui Liu, Peipei Ma, Lihua Zhan, and Longhui Chen. Achieving springback-free age forming via dislocation-enhanced stress relaxation in Al alloy. *Journal of Materials Science & Technology*, 224:222–238, 2025. doi: 10.1016/j.jmst.2024.11.011.

Yo-Lun Yang. *A study of inelastic/anelastic behaviour and springback of AA7050 alloy in creep age forming*. PhD thesis, Imperial College London, 2017.

Yo-Lun Yang. Competitive hardening dynamics in viscoplastic materials with evolving threshold stress. SSRN preprint, 2026.

Yo-Lun Yang, Zhusheng Shi, Yong Li, Qi Rong, and Rajab Said. Experimental studies and constitutive modelling of anelastic creep recovery during creep age forming. In *Procedia Engineering*, volume 207, pages 275–280, 2017. doi: 10.1016/j.proeng.2017.10.774.

Yo-Lun Yang, Tsai-Fu Chung, Md Sadique Ali, Dilshad, and Pengjing Zhao. The influence of creep ageing on the hardening behavior and microstructure of 7050 aluminum alloy. *Metals*, 13(2):196, 2023. doi: 10.3390/met13020196.

Jiwang Yu, Lihua Zhan, and Youliang Yang. Effects of residual stress on springback in creep age forming of 2219 aluminum alloy double-curvature thin-walled parts. *Metals*, 16(3):269, 2026. doi: 10.3390/met16030269.

C. Zener. *Elasticity and Anelasticity of Metals*. University of Chicago Press, Chicago, 1948.

Lihua Zhan, Jianguo Lin, and Trevor A. Dean. A review of the development of creep age forming: Experimentation, modelling and applications. *International Journal of Machine Tools and Manufacture*, 51:1–17, 2011. doi: 10.1016/j.ijmachtools.2010.08.007.

Jin Zhang, Yunlai Deng, and Xinming Zhang. Constitutive modeling for creep age forming of heat-treatable strengthening aluminum alloys containing plate or rod shaped precipitates. *Materials Science and Engineering: A*, 563:8–15, 2013. doi: 10.1016/j.msea.2012.10.055.

L. W. Zhang, T. J. Bian, H. Li, X. D. Yang, and C. Lei. Stress relaxation aging of 7050 aluminum alloy under elastic and plastic loadings: A perspective from the geometrically necessary dislocations. *Journal of Alloys and Compounds*, 1010:177066, 2025. doi: 10.1016/j.jallcom.2024.177066.

Liwen Zhang, Heng Li, Tianjun Bian, Changhui Wu, Yang Gao, and Chao Lei. Advances and challenges on springback control for creep age forming of aluminum alloy. *Chinese Journal of Aeronautics*, 35(10):8–34, 2022. doi: 10.1016/j.cja.2021.10.019.

Jing-Hua Zheng, Ran Pan, Chen Li, Wei Zhang, Jianguo Lin, and Catrin M. Davies. Experimental investigation of multi-step stress-relaxation-ageing of 7050 aluminium alloy for different pre-strained conditions. *Materials Science and Engineering: A*, 710:111–120, 2018. doi: 10.1016/j.msea.2017.10.066.

Jing-Hua Zheng, Yufeng Jin, Lang Xu, Congze Fan, Wenzhe Song, and Yiwei Chen. Comparative study of creep and stress relaxation behaviour during ageing of 7050 aluminum alloy. *Metals*, 13(4):778, 2023. doi: 10.3390/met13040778.

Jinghua Zheng, Catrin M. Davies, and Jianguo Lin. Comparison of creep deformation rates during load and strain controlled multi-step creep ageing tests on AA7050. In *AIP Conference Proceedings*, volume 1892, page 160003, 2017. doi: 10.1063/1.5008178.

Qingheng Zhou, Xuelian Xiao, Kaihao Wang, Yong Li, and Wenbin Zhou. Investigation of the deformation and microstructural evolution mechanisms during multi-step stress-relaxation ageing of 7050 aluminium alloy. *Materials Science and Engineering: A*, 976:150996, 2026. doi: 10.1016/j.msea.2026.150996.

Guillaume Zumpicchiat, Benoit Tanguy, Pierre Gavoille, Valérie Vandenberghe, and Julien Vidal. In-reactor stress relaxation of 3-point bending CW-316 samples: Experiments and modelling. *Journal of Nuclear Materials*, 616:155990, 2025. doi: 10.1016/j.jnucmat.2025.155990.

Supplementary Files

This is a list of supplementary files associated with this preprint. Click to download.

- SupplementaryPaperEv33b.pdf